The Astrophysical Journal, 927:218 (27pp), 2022 March 10 https://doi.org/10.3847/1538-4357/ac49e0

ALMA Survey of Orion Planck Galactic Cold Clumps (ALMASOP): A Hot Corino Survey toward Protostellar Cores in the Orion Cloud

Shih-Ying Hsu[1,2], Sheng-Yuan Liu[2], Tie Liu[3], Dipen Sahu[2], Chin-Fei Lee[2], Kenichi Tatematsu[4,5], Kee-Tae Kim[6,7], Naomi Hirano[2], Yao-Lun Yang[8], Doug Johnstone[9,10], Hongli Liu[11], Mika Juvela[12], Leonardo Bronfman[13], Huei-Ru Vivien Chen[14], Somnath Dutta[2], David J. Eden[15], Kai-Syun Jhan[1,2], Yi-Jehng Kuan[16,2], Chang Won Lee[6,7], Jeong-Eun Lee[17], Shanghuo Li[18], Chun-Fan Liu[2], Sheng-Li Qin[19], Patricio Sanhueza[20,21], Hsien Shang[2], Archana Soam[22,23], Alessio Traficante[24], and Jianjun Zhou[25]

[1] National Taiwan University (NTU), No. 1, Section 4, Roosevelt Road, Taipei 10617, Taiwan (R.O.C.); seansyhsu@gmail.com
[2] Institute of Astronomy and Astrophysics, Academia Sinica, No.1, Sec. 4, Roosevelt Road, Taipei 10617, Taiwan (R.O.C.); syliu@asiaa.sinica.edu.tw
[3] Key Laboratory for Research in Galaxies and Cosmology, Shanghai Astronomical Observatory, Chinese Academy of Sciences, 80 Nandan Road, Shanghai 200030, People's Republic of China
[4] Nobeyama Radio Observatory, National Astronomical Observatory of Japan, National Institutes of Natural Sciences, 462-2 Nobeyama, Minamimaki, Minamisaku, Nagano 384-1305, Japan
[5] Department of Astronomical Science, The Graduate University for Advanced Studies, SOKENDAI, 2-21-1 Osawa, Mitaka, Tokyo 181-8588, Japan
[6] Korea Astronomy and Space Science Institute (KASI), 776 Daedeokdae-ro, Yuseong-gu, Daejeon 34055, Republic of Korea
[7] University of Science and Technology, Korea (UST), 217 Gajeong-ro, Yuseong-gu, Daejeon 34113, Republic of Korea
[8] Department of Astronomy, University of Virginia, Charlottesville, VA 22904, USA
[9] NRC Herzberg Astronomy and Astrophysics, 5071 West Saanich Road, Victoria, BC, V9E 2E7, Canada
[10] Department of Physics and Astronomy, University of Victoria, Victoria, BC, V8P 5C2, Canada
[11] Department of Astronomy, Yunnan University, Kunming 650091, People's Republic of China
[12] Department of Physics, P.O.Box 64, FI-00014, University of Helsinki, Finland
[13] Departamento de Astronomía, Universidad de Chile, Casilla 36-D, Santiago, Chile
[14] Department of Physics and Institute of Astronomy, National Tsing Hua University, Hsinchu, 30013, Taiwan (R.O.C.)
[15] Astrophysics Research Institute, Liverpool John Moores University, iC2, Liverpool Science Park, 146 Brownlow Hill, Liverpool, L3 5RF, UK
[16] Department of Earth Sciences, National Taiwan Normal University, Taipei, Taiwan (R.O.C.)
[17] School of Space Research, Kyung Hee University, 1732, Deogyeong-Daero, Giheung-gu Yongin-shi, Gyunggi-do 17104, Republic of Korea
[18] Korea Astronomy and Space Science Institute, 776 Daedeokdae-ro, Yuseong-gu, Daejeon 34055, Republic of Korea
[19] Department of Astronomy, Yunnan University, and Key Laboratory of Astroparticle Physics of Yunnan Province, Kunming, 650091, People's Republic of China
[20] National Astronomical Observatory of Japan, National Institutes of Natural Sciences, 2-21-1 Osawa, Mitaka, Tokyo 181-8588, Japan
[21] Department of Astronomical Science, SOKENDAI (The Graduate University for Advanced Studies), 2-21-1 Osawa, Mitaka, Tokyo 181-8588, Japan
[22] Indian Institute of Astrophysics, II Block, Koramangala, Bengaluru 560034, India
[23] SOFIA Science Center, USRA, NASA Ames Research Center, M.S.-12, N232, Moffett Field, CA 94035, USA
[24] INAF-IAPS, via Fosso del Cavaliere, 100. I-00133, Rome, Italy
[25] Xinjiang Astronomical Observatory, Chinese Academy of Sciences 150 Science 1-Street, 830011 Urumqi, People's Republic of China
Received 2021 August 9; revised 2022 January 4; accepted 2022 January 7; published 2022 March 17

Abstract

The presence of complex organic molecules (COMs) in the interstellar medium is of great interest since it may link to the origin and prevalence of life in the universe. Aiming to investigate the occurrence of COMs and their possible origins, we conducted a chemical census toward a sample of protostellar cores as part of the Atacama Large Millimeter/submillimeter Array Survey of Orion Planck Galactic Cold Clumps project. We report the detection of 11 hot corino sources, which exhibit compact emissions from warm and abundant COMs, among 56 Class 0/I protostellar cores. All of the hot corino sources discovered are likely Class 0, and their sizes of the warm region (>100 K) are comparable to 100 au. The luminosity of the hot corino sources exhibits positive correlations with the total number of methanol and the extent of its emissions. Such correlations are consistent with the thermal desorption picture for the presence of hot corinos and suggest that the lower-luminosity (Class 0) sources likely have a smaller region with COM emissions. With the same sample selection method and detection criteria being applied, the detection rates of the warm methanol in the Orion cloud (15/37) and the Perseus cloud (28/50) are statistically similar when the cloud distances and the limited sample size are considered. Observing the same set of COM transitions will bring a more informative comparison between the cloud properties.

Unified Astronomy Thesaurus concepts: Astrochemistry (75); Interstellar molecules (849); Star forming regions (1565); Low mass stars (2050); Protostars (1302)

Supporting material: machine-readable table

1. Introduction

The presence of complex organic molecules (COMs), those organic molecules consisting of six or more atoms, in the interstellar medium (ISM) is particularly of great interest since it may link to the origin and prevalence of organic matter and even life in the universe. Saturated complex organic molecules (also often referred to as complex organic molecules, COMs, interstellar COMs, or iCOMs) have been discovered in various star-forming environments, including prestellar cores (e.g., L1689B; Bacmann et al. 2012), protostellar cores (e.g., IRAS 16293–2422 A and B; Bottinelli et al. 2004; Kuan et al. 2004; Huang et al. 2005),

outflows (e.g., L1157; Arce et al. 2008), and most recently protostellar disks (e.g., HH-212 and V883 Ori3; Lee et al. 2017, 2019b). In particular, hot corino sources are identified by localized zones, which surround low- or intermediate-mass forming stars and harbor warm (∼100 K), abundant (relative column density with respect to molecular hydrogen $X > 10^{-8}$), and compact (∼100 au) COM emissions (Cazaux et al. 2003). Since its first identification in 2004 (Ceccarelli 2004), to date only about a couple tens of hot corino sources have been discovered, including, for example, IRAS 16293–2422 B (Kuan et al. 2004; Huang et al. 2005), B335 (Imai et al. 2016), HH-212 (Codella et al. 2016; Lee et al. 2017, 2019a), NGC 1333 IRAS 4A1 (Sahu et al. 2019), and BHR–71 IRS1 (Yang et al. 2020).

Recently, there have emerged studies investigating the statistical nature of COM emissions toward selected samples of protostellar cores. Belloche et al. (2020) observed 26 solar-type star-forming regions, including 22 Class 0 and four Class I protostars, under the project "Continuum And Lines in Young ProtoStellar Objects (CALYPSO)" conducted with Plateau de Bure Interferometer. Based on the chemical differentiation in multiple systems, they raised the question of whether the hot corino phase is a common stage of star formation. van Gelder et al. (2020) investigated COM emission on the scale of ∼100 au toward seven Class 0 protostellar cores, including four sources in the Perseus Barnard 1 cloud and three sources in the Serpens Main region. They found three of these seven sources to be COM-rich and among these three sources similar abundance ratios of COMs, including deuterated methanol (CH_2DOH), methyl formate ($HCOOCH_3$), and dimethyl ether (CH_3OCH_3), with respect to CH_3OH. Since such comparable abundance ratios have also been reported toward two other COM-rich sources in different clouds: IRAS 16293–2422 B in the Ophiuchus cloud and HH 212 in the Orion cloud, van Gelder et al. (2020) suggested that the abundances of most O-bearing COMs are similar among different star-forming regions at their prestellar stages. For a few COMs having varying abundance ratios with respect to CH_3OH, such as acetaldehyde (CH_3CHO) and ethanol (C_2H_5OH), van Gelder et al. (2020) on the other hand suggested that they were affected by the local environment of the parent cloud. Toward the same sample of van Gelder et al. (2020), the similar abundances of N-bearing molecules with respect to isocyanic acid (HNCO) suggest a shared chemical history (Nazari et al. 2021). Yang et al. (2021) carried out a survey of COMs toward 50 protostars in the Perseus cloud. The sample was selected to have the following properties: (1) the central source is Class 0/I, (2) the bolometric luminosity $L_{\rm bol} > 1 L_{\odot}$ (except for B1–5), and (3) the envelope mass $M_{\rm env} > 1 M_{\odot}$ to ensure the association of a substantial amount of molecular gas. They reported 28 detections of CH_3OH emission among 50 embedded Class 0/I protostars, and also suggested a possible chemical relation between methanol (CH_3OH) and methyl cyanide (CH_3CN).

To investigate the occurrence of COM emissions and their possible origins, we conducted a chemical census toward a sample of protostellar cores as part of the Atacama Large Millimeter/submillimeter Array (ALMA) Survey of Orion Planck Galactic Cold Clumps (ALMASOP) project. Starting with a sample of Planck Galactic cold clumps (Planck et al. 2016) in the Orion Molecular Complex, which are cold and dense and likely star-forming dust condensations, we made a series of observations and studies (Tatematsu et al. 2017; Liu et al. 2018; Yi et al. 2018; Eden et al. 2019; Kim et al. 2020; Tatematsu et al. 2020). Based on their 850 μm continuum and N_2D^+ emission, we selected 72 clumps as the ALMASOP observation targets. Some of these 72 targets harbor more than one core, which may be starless, prestellar, or protostellar (Dutta et al. 2020). See Hsu et al. (2020), Dutta et al. (2020), and Sahu et al. (2021) for more details about the project and the sample selection.

Hsu et al. (2020) reported the identification of four hot corino sources, which are G211.47–19.27S (HOPS–288), G208.68–19.20N1 (HOPS–87) , G210.49-19.79W–A (HOPS–168), and G192.12–11.10, based on the observational data obtained from the Atacama Compact Array (ACA), a 7 m array of ALMA. These four hot corinos harbor emission from CH_3OH and other oxygen-bearing COMs (in G211.47–19.27S and G208.68–19.20N1) as well as NH_2CHO (in G211.47–19.27S), which is of prebiotic interests. Although the spatial resolution achieved with the ACA was not sufficient to resolve most of the molecular emission distributions, the large line widths (4–9 km s^{-1}) and high rotational temperatures (>100 K) of the detected COMs suggest that they likely reside in the hotter and innermost region immediately surrounding the protostars. The occurrence of hot corino sources was about 8%, based on the detection of warm (>100 K) methanol among the 48 Class 0/I protostellar cores identified in the ACA-only data.

In this paper, Section 2 introduces the observation of the ALMASOP project. We report the detection of 11 hot corino sources among 56 Class 0/I protostellar cores from the combined data of ALMASOP in Section 3. Section 4 presents our spectral energy distribution (SED) modeling, based on which we infer the thermal structure and the extent of the warm region (>100 K) in these sources. In Section 5.1, we discuss the SED ranges and the classifications (i.e., Class 0/I) of the detected hot corinos. We show the correlation between the luminosity and the detection of hot corinos (Section 5.2.1) and demonstrate how sensitivity impacts the detection rate of hot corinos (Section 5.2.2). We also compare the detection rate of warm methanol, an indicator of the occurrence of hot corinos, in our survey toward the Orion cloud and that toward the Perseus cloud (Section 5.2.3). We discuss the chemical relations between the identified organic molecules based on their column densities (Section 5.3), and finally summarize our findings in Section 6.

2. Observations

The observations toward the 72 targets of the ALMASOP project were carried out with both the 12 m array (in two configurations: C43–5 and C43–2 represented, respectively, by TM1 and TM2) and the 7 m array (ACA) of ALMA in the ALMA Cycle 6 operation (#2018.1.003.2.S, PI: Tie Liu). Following the successful identifications of the hot corino sources with the ACA data in Hsu et al. (2020), we further combined the ALMA and ACA data for gaining a better angular resolution. The imaging was carried out using `tclean` in Common Astronomy Software Applications (CASA; McMullin et al. 2007) 5.6 with the following parameters: a robust value of 2.0, the thresholds for the spectral cube and the continuum multifrequency synthesis image of 20 mJy and 60 μJy, respectively. The resulting typical angular resolution is 0.″35, which corresponds to about 140 au for a distance of ∼400 pc. The sensitivity of the image reaches ∼2.8 mJy

Table 1
Source Information

Name	Short Name	Cloud	α_{J2000}	δ_{J2000}	L_{bol} ($L_\odot$)	T_{bol} (K)	Class	HOPS Index
G192.12–11.10	G192	λ Orionis	05h32m19.4	+12d49m40.92	9.5 ± 4.0	44 ± 15	0	⋯
G196.92–10.37–A	G196A	λ Orionis	05h44m29.2	+09d08m52.18	⋯	⋯	(0)	⋯
G203.21–11.20W2	G203W2	Orion B	05h53m39.5	+03d22m23.89	0.5 ± 0.3	15 ± 5	(0)	⋯
G205.46–14.56S1–A	G205S1A	Orion B	05h46m07.2	−00d13m30.24	22.0 ± 8.0	44 ± 19	0	HOPS–358
G206.93–16.61W2	G206W2	Orion B	05h41m24.9	−02d18m06.75	6.3 ± 3.0	31 ± 10	0	HOPS–399
G208.68–19.20N1	G208N1	Orion A	05h35m23.4	−05d01m30.60	36.7 ± 14.5	38 ± 13	0	HOPS–87
G208.89–20.04E	G208E	Orion A	05h32m48.1	−05d34m41.46	2.2 ± 1.0	108 ± 25	(I)	⋯
G209.55–19.68N1–B	G209N1B	Orion A	05h35m08.6	−05d55m54.67	9.0 ± 3.7	47 ± 13	0	HOPS–12
G209.55–19.68S1	G209S1	Orion A	05h35m13.4	−05d57m57.89	9.1 ± 3.6	50 ± 15	0	HOPS–11
G210.49–19.79W–A	G210WA	Orion A	05h36m18.9	−06d45m23.55	60.0 ± 24.0	51 ± 20	0	HOPS–168
G211.47–19.27S	G211S	Orion A	05h39m56.0	−07d30m27.62	180.0 ± 70.0	49 ± 21	0	HOPS–288

Note. α_{J2000} and δ_{J2000} are the R.A. and decl., respectively, of the peak position in our combined 1.3 mm continuum observations. T_{bol} and L_{bol} are bolometric temperature and bolometric luminosity adapted from Dutta et al. (2020). The classes of the sources without photometric data at 70 ∼100 μm in Dutta et al. (2020) are marked in parentheses. For the four sources that are not HOPS objects: G192, G196A, and G203W2 are not in the spatial coverage of the HOPS observations; and G208E does not have 24 μm photometric data (Megeath et al. 2012; Fischer et al. 2013).
References. L_{bol}, T_{bol}, and Class: Dutta et al. (2020); HOPS: Furlan et al. (2016).

beam^{-1} and ∼12 μJy beam^{-1} for each channel (1.129 MHz) and the full-band (7.5 GHz) continuum, respectively.

3. Molecule Detection

3.1. Data and Tools

To have a quick search of the presence of COMs, we first extract the spectra at the continuum peak pixel for the protostellar cores from the ALMASOP sample. We select the sources where at least two methanol transitions are detected (signal-to-noise ratio, S/N > 5) and define their emission extent based on the 2D Gaussian fitting of their CH_3OH moment-0 images. The CH_3OH transition we use is at $J = 4 - 3; K_a = 2 - 1; K_c = 3 - 2; E_{up} = 46$ K; and $f_{rest} =$ 218440 MHz (hereafter CH_3OH–46K transition), which is the strongest methanol transition in our spectral windows. We then extract the full spectra within the same extent toward each source. Following similar procedures as Hsu et al. (2020), we use the eXtended CASA Line Analysis Software Suite (XCLASS; Möller et al. 2017) to search for the molecular carrier candidates with its `LineIdentification` function, and to simulate synthetic spectra with input molecular parameters including the excitation temperature (T_{ex}), total column density (N), line width in velocity (δv), and local-standard-of-rest velocity (v_{LSR}). Each (gaseous) molecular component is assumed to be in its individual local thermodynamic equilibrium. We further use Modeling and Analysis Generic Interface for eXternal numerical codes (MAGIX), a package of XCLASS, to optimize the above parameters. The optimization algorithms in MAGIX we use are "Bees algorithms" and "Levenberg–Marquardt (LM) algorithms." The former is a swarm algorithm providing a good overview for all parameter combinations within given ranges. The latter is also known as the "damped least-squares nonlinear method" for finding local minima in nonlinear least-squares problems. To have a first estimation, we make individual fittings for each molecular species with the Bees algorithm, and the range of T_{ex} is limited to be (0, 400). We then run overall fittings for all species simultaneously with the Bees algorithm and LM algorithm for each source to take into account blending of lines. We assume the emission size of all species to be the (2D Gaussian) extent of the CH_3OH–46K transition deconvolved by the beam size.

For molecules detected with only one transition, we assume their T_{ex} to be 100 K, the typical temperature of a hot corino. The estimate of column density (N) in these cases hence may not be less precise.

3.2. Results

The combined data (TM1+TM2+ACA) of ALMASOP, with a higher angular resolution, resolve more protostellar cores compared to the ACA data. Consequently, Dutta et al. (2020) reported the identification of 56 Class 0/I protostellar objects. Among the 56 protostellar cores, we find 11 sources with at least two CH_3OH transitions including at least one transition with upper energy $E_{up} > 100$ K getting detected at a level above 5σ. They are G192, G196A, G203W2, G205S1A, G206W2, G208N1, G208E, G209N1B, G209S1, G210WA, and G211S. See Table 1 for their corresponding full names in the ALMASOP observation. Table 1 lists the parent clouds, coordinates, bolometric luminosity, temperature, and classifications of the 11 sources. Seven of these 11 sources were observed by the Herschel Orion Protostar Survey (HOPS), and the correspondence is listed in Table 1. See Appendix A for more details about the 11 sources. Tables B1–B11 display the molecular parameters (i.e., T_{ex}, N, δv, and v_{LSR}) and their errors estimated by the Markov Chain Monte Carlo method in XCLASS of these 11 sources. Figure set B1 shows the spectra and the identified transitions for each source (see Figure B1 for an example). The emission region of the detected COMs, such as methanol and methyl formate, based on their integrated intensity (moment-0) images, are mostly unresolved or marginally resolved, as demonstrated in Figures B2 and B3, except for a few low-excitation transitions.

Based on the presence of compact (a few hundred astronomical unit), warm ($T_{ex} > 100$ K) and abundant ($X > 10^{-8}$) CH_3OH, we consider these 11 cores to be hot corinos. We detect toward them in total 36 molecules, including simple diatomic species such as carbon monoxide isotopologues (CO and $C^{18}O$), simple organics such as formaldehyde isotopologues (H_2CO and D_2CO), and COMs such as methanol isotopologues (CH_3OH, CH_2DOH, $^{13}CH_3OH$, and $CH_3\,^{18}OH$), acetaldehyde isotopologues

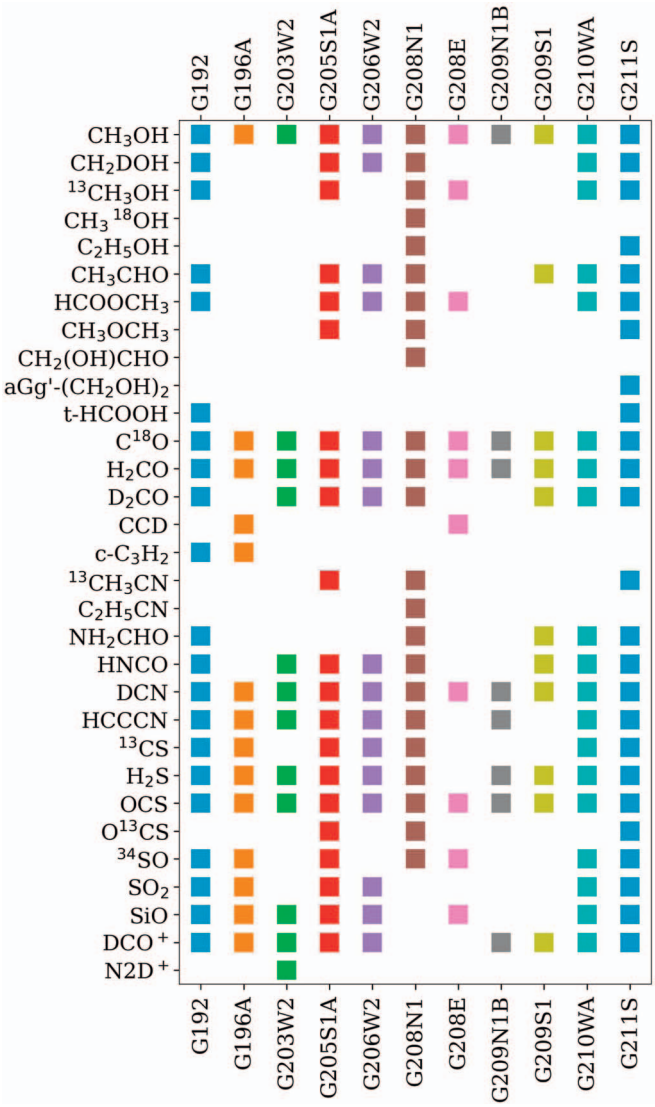

Figure 1. Summary of the molecular detection in each source.

(CH_3CHO and CH_3CHD), methyl formate ($HCOOCH_3$), ethanol (C_2H_5OH), ^{13}C substituted methyl cyanide ($^{13}CH_3CN$), formamide (NH_2CHO), etc. See Table B12 for a complete list of the molecular species and their detected transitions.

Figure 1 summarizes the occurrence of the identified molecules in the 11 sources. There are three sources (i.e., G203W2, G209N1B, and G196A) harboring only one COM, which is CH_3OH. Their weaker continuum emission, corresponding to lower H_2 column densities among the sample, may have prevented the detection of other COMs toward them, should other COMs bear similar fractional abundances as in the stronger sources.

Among these 11 sources, four of them were previously reported as hot corinos in Hsu et al. (2020), namely G192, G208N1, G210WA, and G211S. For the methanol detected in the combined data (TM1+TM2+ACA) of these four sources, their T_{ex} is higher, N is larger, and δv is larger than for those detected in the ACA-only data. The comparison suggests that the combined data enables better detection of methanol from more compact, denser, hotter, and perhaps inner or more turbulent regions.

4. Spectral Energy Distribution Modeling

Aiming to infer the physical structure and the potential origin of COM emissions in our hot corino sources, we carried out SED modeling and obtain the YSO models that may best describe the sources. At the protostellar stage, the short-wavelength radiation emitted by the central protostar and the accretion shock are absorbed and re-emitted by the dust in the disk and envelope with its SED peaking at $\sim$100 μm (Furlan et al. 2016).

4.1. Data

The archival SED data of the 11 sources collected by Dutta et al. (2020) cover from 3.6 μm to 870 μm. These data were extracted from the UKIRT Infrared Deep Sky Survey (UKIDSS; Lawrence et al. 2007), the Spitzer Space Telescope Survey of Orion A-B (Megeath et al. 2012), the Wide-field Infrared Survey Explorer (WISE; Wright et al. 2010), the AKARI/IRC All–Sky Survey Point Source Catalogue, the AKARI/FIS All–Sky Survey Bright Source Catalogue (Ishihara et al. 2010; Oyabu 2010), HOPS (Stutz et al. 2013; Tobin et al. 2015), the Atacama Pathfinder Experiment (APEX; Stutz et al. 2013), and the 850 μm JCMT/SCUBA2 observations by Yi et al. (2018). All of the flux data can be found in Table 6 of Dutta et al. (2020) and shown in Figure C1. See Table C1 for more information of the archival SED data points including their representative wavelengths and apertures.

On top of these SED data points, we append two data points at 1.3 mm based on the continuum images made with the ALMASOP ACA-only data and the combined data (TM1+TM2+ACA). We extracted the flux density at the emission peak on the 1.3 mm continuum images within an aperture that is the same as the beam size (Table A2).

4.2. Tools and Methods

We employed the SED Fitter[25] (Robitaille et al. 2007) for deriving the YSO models that best match the observed SED data points. In the SED Fitter, users have to provide a grid of SED models, a range of foreground extinction (A_V), a range of source distance (D), a list of observed SED data points (flux and the corresponding uncertainty), and the filter response and the aperture of the observation for each SED data point. The SED Fitter will evaluate the χ^2 from the observed flux and the modeled flux under a combination of an SED grid model, A_V, and D, and list the best combinations of parameters with the minimum χ^2 values. In our study, the range of A_V was set to [0, 250] mag, and the distance D was fixed to be 398, 404, and 404 pc, respectively, for sources in the Orion A, Orion B, and λ Orionis clouds (Kounkel et al. 2018).

We adopted the model grid published by Robitaille et al. (2006; hereafter "R06 grid"), which contains the SEDs of 200,000 axis-symmetric 2D YSO models covering a wide range of stellar masses (from 0.1 to 50 $M_\odot$) and evolutionary ages (from 10^3 to 10^7 yr). The SED of each YSO model was produced by the HO-CHUNK package[26] (Whitney et al. 2003), a Monte Carlo code simulating the radiation transfer of YSO models. The physical structural setup of the YSO model in the HO-CHUNK package includes a central star, an accretion disk, an envelope, and an optional outflow cavity, and each of them has its corresponding parameters.

[25] https://sedfitter.readthedocs.io/en/stable/
[26] https://gemelli.colorado.edu/~bwhitney/codes/codes.html

In the R06 grid, there are 14 model parameters, including stellar mass ($M_\star$), stellar radius ($R_\star$), stellar temperature ($T_\star$), envelope accretion rate ($\dot{M}_{\rm env}$), envelope outer radius ($R_{\rm env}^{\rm outer}$), cavity density ($\rho_{\rm cav}$), cavity opening angle (θ), disk mass ($M_{\rm disk}$), disk outer radius ($R_{\rm disk}^{\rm outer}$), inner radius of disk and envelope ($R_{\rm disk}^{\rm inner}$), disk accretion rate ($\dot{M}_{\rm disk}$), disk scale height factor ($z_{\rm disk}^{\rm scale}$), disk flaring power component (B), and ambient density ($\rho_{\rm amb}$). Robitaille et al. (2006) further introduced an additional parameter into the YSO model, the stellar age ($t_\star$). While some of these parameters (such as stellar age) are uniformly sampled within their given ranges, there are also parameters that correlate with each other (such as stellar mass and stellar radius). For each set of these parameters, the R06 grid model SEDs are evaluated at 10 different inclination values ($\cos\varphi$) equally ranging from 0.05 to 0.95 and 50 different apertures ranging from 100 to 100,000 au. See Whitney et al. (2003), Robitaille et al. (2006), Robitaille et al. (2007), and the instruction file of the HO-CHUNK for more information.

In addition to the photometric data points, the continuum and molecular line images obtained with ALMASOP readily yield constraints to the acceptable model. Here we briefly introduce these constraints. First, the disk size (disk outer radius) should be less than 140 au due to the fact that there were no clear disk signatures in the $C^{18}O$ $J=2-1$ moment-0 images for all of the hot corino sources (except G192). Second, all of the sources (except G209N1B) have a clear bipolar outflow in their CO $J=2-1$ moment-0 images. The effective opening angle (Θ) of a cavity can be described by the true opening angle (θ) and the inclination angle (φ, where $\varphi=0$ corresponds to an edge-on viewing down the longitudinal axis):

$$\tan\Theta = \frac{\tan\theta}{\cos(90^\circ - \varphi)}. \quad (1)$$

The observed effective opening angle of the outflow ($\Theta^{\rm obs}$) therefore helps constrain the cavity opening angle and the inclination of the YSO model (see Figure C2 and Table C2). Appendix C elaborates in more detail the methods. We applied the SED fitting analysis only to eight sources, including G192, G205S1A, G206W2, G208N1, G209N1B, 209S1, G210WA, and G211S, as the other three targets lack photometric data at the [70–100] μm band, the critical wavelengths for constraining the total luminosity.

4.3. Results

We present in Table C3 the five best-fit YSO models exported by the SED Fitter for each source and examine the common features among these best models for each source:

1. *Central Protostar*: Despite the R06 grid having a wide range of stellar ages (10^3 to 10^7 yr), the best-fit $t_\star$ of the sources are all younger than or comparable to 10^5 yr. This general youth is expected since all of the sources are at their early evolutionary stages based on our original sample selection criteria. The other three stellar parameters, namely $T_\star$, $R_\star$, and $M_\star$, are generally similar among the five best-fit models for each source. In the R06 grid, the luminosity is primarily contributed by the stellar radiation (rather than by the disk accretion), which is likely to constrain "uniquely" the stellar parameters.

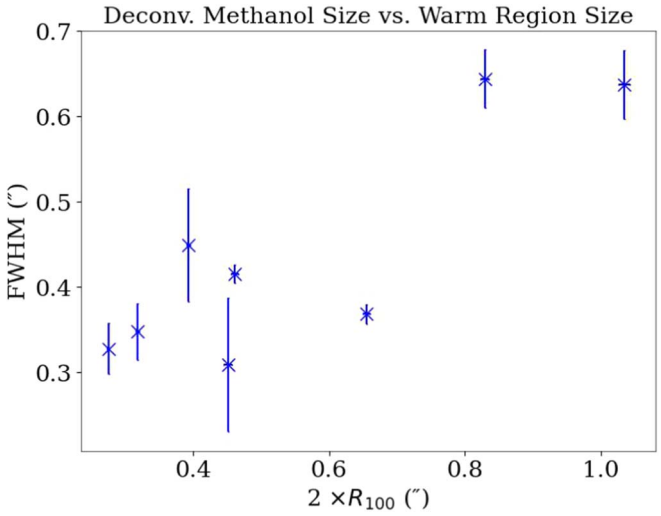

Figure 2. The deconvolved size of methanol vs. the diameter of the 100 K boundary. The methanol transition is the CH_3OH–46 transition, which is the strongest transition in this study.

2. *Disk*: Although the disk sizes (disk outer radius or $R_{\rm disk}^{\rm outer}$) are more diverse than the stellar parameters between the five best-fit models for each source (e.g., 11 au $< R_{\rm disk}^{\rm outer} <$ 127 au for G210WA), all of the disk sizes are below or comparable to the given maximum outer disk radius, 140 au, which is constrained by the lack of velocity gradients in the $C^{18}O$ $J=2-1$ images in most sources, and are significantly smaller than the sizes deduced by Furlan et al. (2016; except for G210WA). The ALMASOP photometric measurements of the 1.3 mm continuum, which traces cool dust at the 100 au scale, likely have helped in constraining the disk sizes.
3. *Envelope and cavity*: In spite of the potential large degeneracy in the cavity opening angle in combination with the wide range of the inclination, the inferred cavity opening angle appears generally constrained for each source (e.g., $2\overset{\circ}{.}51 < \theta < 8\overset{\circ}{.}77$ in G206W2 and $9^\circ < \theta < 11^\circ$ in G209S1).

4.4. Warm Region Sizes in the YSO Models

We further reconstruct the physical model using the 2008 version of the HO-CHUNK code with the best-fit parameters obtained from the SED Fitter despite a few limitations noted below. These limitations are: (1) the version of the HO-CHUNK code for making the R06 grid was released in 2006 but is no longer available; (2) part of the HO-CHUNK R06 model grid parameters, such as the magnetosphere corotation radius, are not advertised, and (3) some input models (e.g., the grain dust model and the stellar photosphere model) used by HO-CHUNK are not directly provided. More details about these limitations and how we mitigate them are given in Appendix C.

While the inferred physical (thermal) structures of the sources are model dependent and the real situation may be far more complicated than what has been assumed in the SED models, the results from our analysis are nevertheless indicative. Figure 2 plots the deconvolved source size of the CH_3OH–46 transition versus the warm region size (>100 K, the typical temperature of a hot corino) inferred from the SED fitting. There exists a positive correlation between the two

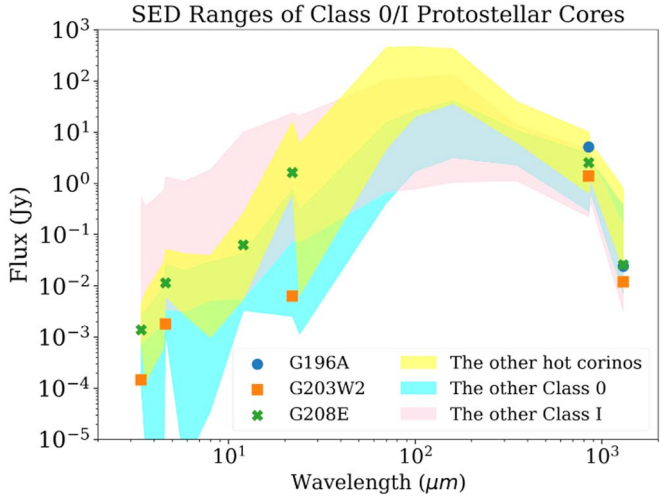

Figure 3. SED ranges of the Class 0/I protostellar cores in ALMASOP. The pink and blue shaded areas represent the Class I and Class 0 protostellar cores that are not hot corinos, respectively. The yellow shaded area represents the hot corinos having [70–160] μm photometric data. The scatters show the photometric data points of the three hot corinos lacking [70–160] μm photometric data. The shaded areas are made by the interpolation based on the 15 wavelengths, where most of the sources have photometric data at. The photometric data are adopted from WISE, Spitzer IRAC, Spitzer MIPS, Herschel PACS, APEX, JCMT/SCUBA2, and ALMASOP. Sources with data at fewer than 10 of the 15 wavelengths are not used. See Table C1 for the references.

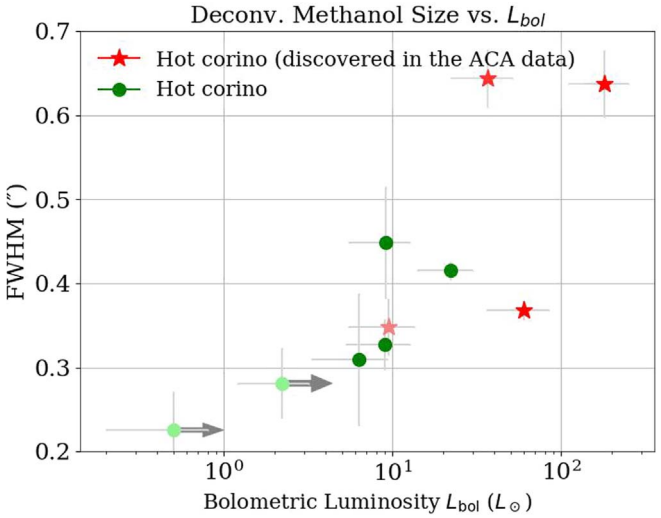

Figure 4. The deconvolved size of the CH_3OH–46K transition vs. the bolometric luminosity (L_{bol}) adapted from Dutta et al. (2020) of the hot corino sources discovered in the ACA-only data (Hsu et al. 2020) and the combined data (this study). Sources without photometric data points at 100 μm are marked in light colors. The arrows along the x-axis mark the sources with L_{bol} lower limits due to their lacking of [70–160] μm photometric data points. G196A is excluded from the plot due to its lack of photometric data in the IR band.

quantities with a ratio on the order of unity, indicating that the YSO model exported by the SED fitting is reflecting a coherent trend seen in the real observations. In addition, the sizes of the warm region are larger than the inferred disk sizes, hinting that the warm regions, where COM emissions originate, extend to the inner envelopes.

5. Discussion

5.1. SED and Classification of Hot Corinos

We report toward our ALMASOP sample the detection of 11 hot corinos, among which 10 were classified as Class 0 and one was classified as Class I by Dutta et al. (2020) based on their bolometric temperatures. G208E, the only Class I hot corino, appears special, as there have been so far only a very limited number of Class I hot corinos reported, namely SVS 13A (Bianchi et al. 2019), Ser-emb 17 (Bergner et al. 2019), L1551 IRS5 (Bianchi et al. 2020), and Ser-emb 11 W likely in Class 0/I transition (Martín-Doménech et al. 2021). We note, however, that the classification of G208E may not be secure. Figure 3 displays the range of SEDs for the Class 0 sources with hot corino detection, without hot corino detection, and the Class I sources in yellow, blue, and pink, respectively. The fact that G208E, marked by green asterisks, lacks the photometric data at the [70–160] μm band where the SED of a (Class 0) protostellar core typically peaks, makes its T_{bol} uncertain. In fact, the photometric fluxes of G208E in the detected bands are all well within the range spanned by the other Class 0 hot corino sources. The tentative steep slope at near-IR (12 and 22 μm) also makes G208E more similar to a Class 0 source. As a result, there may not be any Class I hot corinos among the ALMASOP sample. As discussed in Section 5.2, the COM emission likely originates from the warm (>100 K) inner envelopes, the lack of COM emission in Class I YSOs may be linked to their tenuous envelope remaining around the central YSOs. Future (SED) modeling of the Class I source in our sample may help verify this speculation.

There are two other hot corino sources, G196A and G203W2, with uncertain bolometric luminosity and bolometric temperature due to their lack of [70 ~160] μm photometric data points. Dutta et al. (2020) previously reported that both G196A and G203W2 are Class 0 protostellar cores. Since G196A has only one photometric data point in addition to the ALMASOP band, Dutta et al. (2020) did not report its T_{bol} and L_{bol}. G203W2 was reported with a low bolometric temperature ($T_{bol} = 15$ K; Dutta et al. 2020). However, its SED curve is close to the lower boundary of the hot corino range, and there appears to be no strong evidence for an exceptionally low T_{bol} (Figure 3).

The lack of photometric data points at [70–160] μm also restricts the derivation of L_{bol} in addition to T_{bol} for G203W2 and G208E. As shown in Figure 3, the SED of Class 0/I protostellar cores typically peak at the [70–160] μm band. The flux at the [70–160] μm band can be orders of magnitude stronger than the other bands. Therefore, the reported L_{bol} values of these sources (G203W2 and G208E) may be severely underestimated and represent the lower limits.

5.2. Detection Rate of Hot Corinos

5.2.1. Luminosity and Warm Region in Hot Corino

In the contemporary paradigm of hot corinos, the COMs frozen in grain mantles get thermally desorbed due to ice sublimation at ~100 K (see, for example, Garrod & Herbst 2006; Garrod et al. 2008; Herbst & van Dishoeck 2009). One may expect that a protostellar core with a higher luminosity may warm up a broader region, which leads to a wider extent of COMs. Figure 4 displays the bolometric luminosity (L_{bol}) versus the deconvolved size of the CH_3OH–46K transition. The extent of methanol, the simplest COM, indeed correlates positively with the bolometric luminosity.

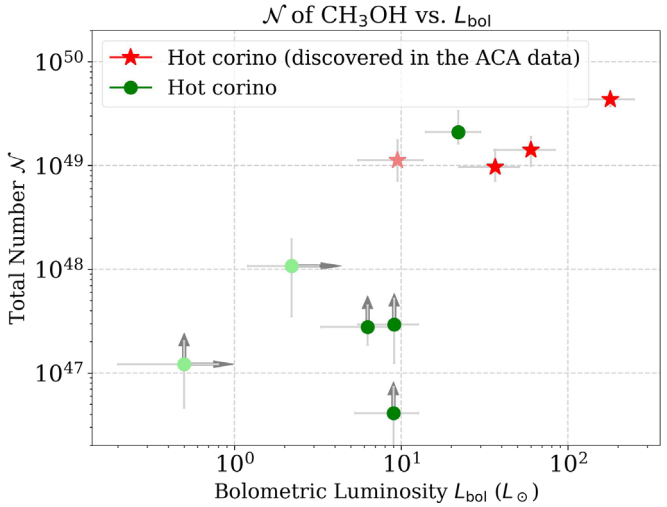

Figure 5. The total number of methanol molecules within the source size vs. bolometric luminosity (L_{bol}) adapted from Dutta et al. (2020) of the hot corino sources discovered in the ACA-only data (Hsu et al. 2020) and the combined data (this study). Sources without photometric data points at 100 μm are marked in light colors. The arrows along the x-axis mark the sources with L_{bol} lower limits due to their lacking of [70–160] μm photometric data points. The methanol column densities are derived by [$^{13}CH_3OH$]×50. For the sources without $^{13}CH_3OH$, we use [CH_3OH] and mark them with the arrows along the y-axis. G196A is excluded from the plot due to its lack of photometric data in the IR band.

Simulations have suggested that methanol mainly forms during the prestellar phase (Drozdovskaya et al. 2015; Coutens et al. 2020). If the fractional abundance of methanol is comparable among the hot corinos, one would also expect that the total number of gas-phase methanol is positively correlated with the bolometric luminosity based on the correlation between the extent of methanol and the bolometric luminosity. We derive the total number of molecules ($\mathcal{N}$) within the emission extent with: $\mathcal{N} = N \times (\theta_S \times D)^2$, where N is the column density, θ_S is the source size, and D is the distance. Figure 5 presents the total number of methanol molecules derived from the (rescaled) column densities and the bolometric luminosities of the hot corino sources. We use $^{13}CH_3OH$ with $^{12}C/^{13}C = 50$ (Kahane et al. 2018) to derive the methanol column density, given the main isotopologue (CH_3OH) is likely optically thick (see Section 5.3.1 for further explanation). The total number of methanol molecules displays a positive correlation with the bolometric luminosity. The three sources (G203W2, G208E, and G209N1B) with lower limits in L_{bol} and/or N (illustrated by the arrows in Figure 5) are consistent with the trend as well.

5.2.2. Sensitivity and Hot Corino Detection

We further plot the bolometric luminosity (L_{bol}) and the bolometric temperature (T_{bol}) adapted from Dutta et al. (2020) in Figure 6. The bolometric luminosities of Class 0 hot corino sources are relatively high compared to the other Class 0 protostellar cores at similar bolometric temperature. The two sources G203W2 and G208E with lower limits in their bolometric luminosity are consistent with this trend as well.

In Hsu et al. (2020), we reported the detection of four hot corino sources based on the presence of warm methanol with the ACA data of ALMASOP. These hot corino sources in general have high bolometric luminosities ($\gtrsim$30 $L_\odot$; red asterisks in Figure 6). In this study with the combined data, we detect warm methanol toward seven additional protostellar cores, which have intermediate luminosities (∼10–30 $L_\odot$; green dots in Figure 6). The increase of detected hot corino sources may be mainly attributed to the sensitivity of the observations. Since Hsu et al. (2020) and this study use the same set of methanol transitions for detection, we can simply compare their sensitivities by the threshold in brightness temperature and the beam filling factor (η) defined by the FWHM of the source size (θ_S) and the half-power beam width (HPBW) of the synthesized beam (θ_A) via:

$$\eta = \frac{\theta_S^2}{\theta_A^2 + \theta_S^2}. \quad (2)$$

The extent of the methanol component in ACA data is unresolved, so the source size in ACA data is assumed to be as compact as that in the combined data. The current threshold in brightness temperature is about 40 times higher than that of Hsu et al. (2020), which requires a higher molecular abundance for the detection. In contrast, the beam filling factor of this study is about 300 times higher than that of Hsu et al. (2020), leading to much less beam dilution and greater ease of detection. The combined effect results in an increased detection rate of warm methanol from 8% in Hsu et al. (2020) to 20% in this work.

Based on the above premise, the number of detected hot corino sources and the detection rates may simply reflect the line sensitivity (for detecting COM emission) and its level as compared with the continuum sensitivity (for detecting protostellar cores) of the observations. For the other Class 0 protostellar cores that have relatively low luminosities (∼1–10 $L_\odot$; blue crosses), their warm regions may be relatively small, and hence their COM emission resulting from thermal desorption would be just too weak to be detected even with our combined data. It is possible that we may find low-luminosity sources harboring COMs when observed with higher sensitivity observations. An example is B335 (Imai et al.2016), a recently reported hot corino source with a relatively low luminosity (∼0.7 $L_\odot$ at 100 pc; Evans et al. 2015) as compared to our hot corino sample. Note that its bolometric luminosity will be rescaled to 1.9 $L_\odot$ if the distance reported by Watson (2020), 164.5 pc, is adopted. With deeper observations, there are indeed COM emissions detected in B335 (Imai et al.2016).

5.2.3. Comparisons between ALMASOP and PEACHES

We further compare the detection rate of warm methanol in ALMASOP with that found by PEACHES, which is a census of COMs conducted with ALMA toward embedded protostars in the Perseus cloud by Yang et al. (2021). As indicated in Table 2, the apparent detection rate of warm methanol in PEACHES is roughly 2.5 times higher than that in ALMASOP. Here we discuss two factors affecting the detection rate of warm methanol:

1. *Methanol line detection criteria*: Since ALMASOP has a similar sensitivity to that of PEACHES, which is ∼0.5 K, the S/N threshold for a line detection in ALMASOP (5σ) is higher than that (3σ) in PEACHES. A weak methanol detection in PEACHES may be considered as a non-detection in this study.
2. *Sample selection*: The sample selection of PEACHES follows Higuchi et al. (2018), which excludes YSOs with

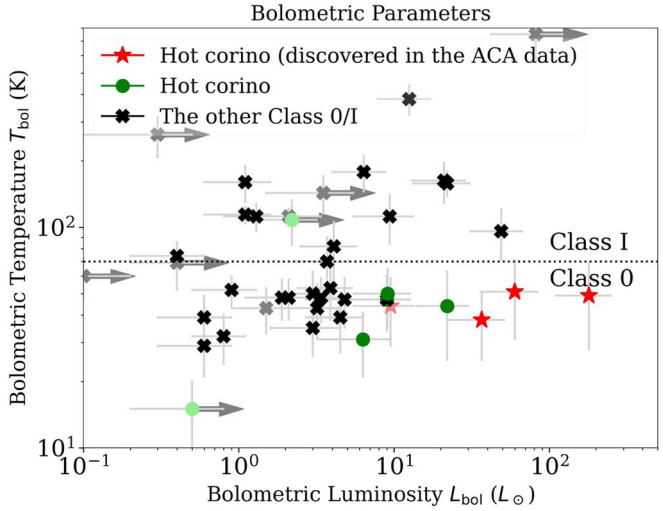

Figure 6. Bolometric temperature (T_{bol}) vs. bolometric luminosity (L_{bol}) adapted from Dutta et al. (2020) of protostellar cores. The sample includes hot corino sources discovered in the ACA-only data (Hsu et al. 2020) and the combined data (this study) and the other Class 0/I protostellar cores imaged by ALMASOP. Sources without photometric data points at 100 μm are illustrated by light colors. The markers with arrows represent the lower limits of the sources lacking [70–160] μm photometric data points. G196A is excluded due to the lack of photometric data in the IR band.

Table 2
Observational Parameters and Detection Rates

	ALMASOP		PEACHES
Cloud	Orion		Perseus
Distance	∼400 pc		∼300 pc
Beam size	∼6″	∼0″.35	∼0″.45
Beam size (au)	∼2500	∼145	∼135
Sensitivity (mJy beam^{-1})	28	2.5	6
Sensitivity (K)	0.02	0.5	0.5
Detection S/N	3	5	3
Threshold (K)	0.06	2.5	1.5
Beam filling factor	0.0046	0.58	0.55
#(Class 0/I)	48	56 (37)	50
#(CH_3OH)	4	11 (15)	28
P(CH_3OH)	8%	20% (41%)	56%

Note. Number of sources under PEACHES sample selection method ($L_{bol} > 1\ L_\odot$) and line detection criteria (3σ) are given in parentheses.
References. PEACHES: Yang et al. (2021); Distance: Kounkel et al. (2018), Ortiz-León et al. (2018),Zucker et al. (2020).

$L_{bol} < 1\ L_\odot$. In ALMASOP, the hot corinos are the Class 0 protostellar cores with high luminosity. Applying the same sample selection method, the total number of protostellar cores in ALMASOP will decrease, and the detection rate of hot corinos will increase correspondingly.

To clarify the influence of these two factors, we also append the hot corino candidates under the same line detection criteria and apply the same sample selection method as PEACHES. We find nine additional Class 0/I protostellar cores where at least one methanol transition is detected at 3σ (see Table A3 for the list). Including those "potential hot corinos" and leaving out all sources fainter than 1 $L_\odot$ in the parent sample for calculating the statistics, the detection rate of hot corinos in ALMASOP becomes 15 out of 37, which remains less than the value (28 out of 50) in PEACHES. The distance difference between the two clouds may contribute to the small difference in the detection rate. Overall, the two rates are statistically similar due to the limited sample size. Observing the same set of methanol (or other COM) transitions will mitigate the problem and enable a fair comparison of the detection rate, which may be indicative of the cloud properties and/or evolutionary stage.

Finally, we note that the dust continuum opacity may prevent the detection of molecular line emissions (e.g., Sahu et al. 2019; De Simone et al. 2020). The detection rates of hot corinos in both ALMASOP and PEACHES are therefore possibly underestimated.

5.3. Complex Organic Molecules in Protostellar Cores

5.3.1. Isotope Ratios of Methanol: $^{12}C/^{13}C$, $^{16}O/^{18}O$, and D/H,

In this section we explore the possible correlations between the column densities of COMs in the hot corinos. A good estimation of the methanol column density is important for performing the comparison with other COMs. Figure 7(a) shows the column densities of CH_3OH and $^{13}CH_3OH$. The isotope $^{12}C/^{13}C$ ratio derived from fitting the observed positive correlation with a linear proportional function is four, an order of magnitude lower than the nominal local ISM value of ∼70 (Wirström et al. 2011) and ∼50 in the Orion cloud (Kahane et al. 2018). The low $^{12}C/^{13}C$ ratio for our hot corino sources most likely suggests high optical depths of the main CH_3OH isotopologue, similar to those reported in the literature (Zapata et al. 2013 for IRAS 16293B; Lee et al. 2019a for HH-212; Hsu et al. 2020 for G211S).

A high optical depth of CH_3OH may have also led to the low $[CH_3OH]/[CH_3^{18}OH]$ value of $11.9^{+3.6}_{-3.5}$ seen in G208N1, which is the only source with $CH_3^{18}OH$ detected among the 11 hot corinos. This $[CH_3OH]/[CH_3^{18}OH]$ value in G208N1 is significantly lower than 562 ± 221 in the hot corino source IRAS 16293A (Manigand et al. 2020), 181 in the hot core sources Sgr B2(N2) (Müller et al. 2016), and 560 ± 25 in the local ISM (Wilson & Rood 1994). Considering that CH_3OH is indeed optically thick and factoring the $^{12}C/^{13}C$ ratio ranging between 50 and 77 (Wilson & Rood 1994; Wirström et al. 2011; Kahane et al. 2018), we scale the column density of $^{13}CH_3OH$ accordingly and find that the $^{16}O/^{18}O$ ratio of methanol in G208N1 becomes 127–190. It appears much closer, though still less than the local ISM value, implying possibly an underestimate of the $^{13}CH_3OH$ column density.

Bianchi et al. (2020) has reported high opacity in a ^{13}C substituted methanol transition ($^{13}CH_3OH$) at E_{up}=48 K toward the Class I hot corino L1551 IRS5. We consider that the column densities of $^{13}CH_3OH$ derived in this study are not severely affected by the opacity because, first, the $[^{13}CH_3OH]$ in this study are derived from transitions including those at high upper energies (i.e., E_{up}=162 and 254 K), which are less affected by the opacity, and second, the ratio between the column densities of $^{13}CH_3OH$ and CH_2DOH appears to be similar among the hot corino sources in this study and in the literature (Figure 7). Furthermore, the hot corinos in this study are Class 0, which are different from those in Bianchi et al. (2020; see Section 5.1).

We also detect deuterated methanol (CH_2DOH), another isotopologue of methanol, in multiple hot corino sources and Figure 7(b) shows their column densities. Figure 7 also shows the data points toward other sources, including hot corino sources HH-212 (Lee et al. 2019a), L483 (Jacobsen et al.

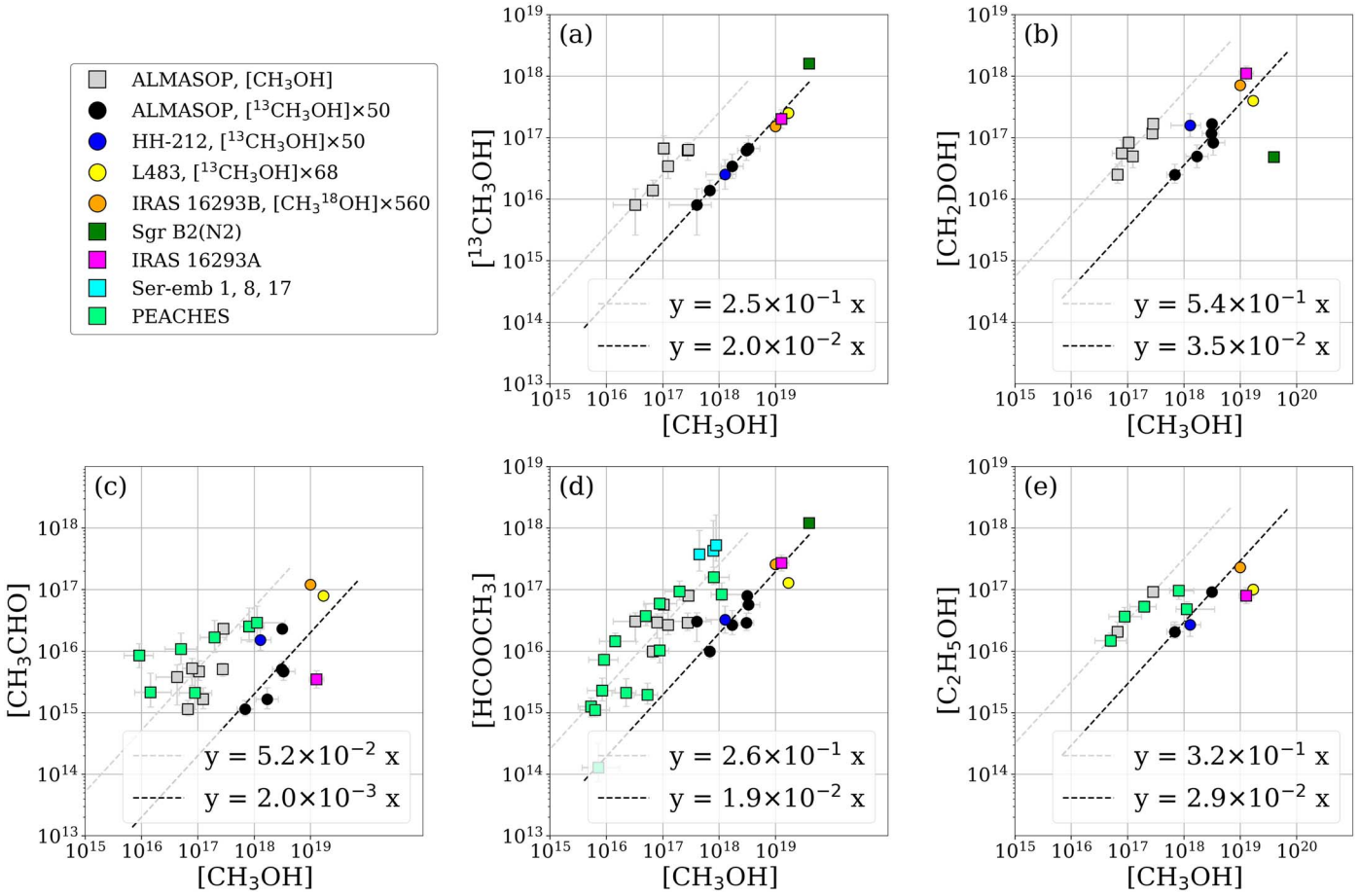

Figure 7. Selected molecular column densities with respect to methanol column densities. Note that the squares, namely for HH-212, L483, and IRAS 16293B, denote that the [CH_3OH] are derived by the corresponding authors from the rare isotopologues. Also note that Sgr B2 (N2) is a hot core, which is a massive protostellar core, and its chemistry mechanism may be different from hot corino chemistry. The black and gray dashed lines are the fit of ALMASOP data (black and gray) by a linear proportional function. The units of both the *x*-axis and *y*-axis are cm^{-2}. References: HH-212 (Lee et al. 2019a), IRAS 16293A (Manigand et al. 2020), IRAS 16293 B (Jørgensen et al. 2018; Persson et al. 2018), L483 (Jacobsen et al. 2019), Ser-emb 1, 8 and 17 (Bergner et al. 2019), Sgr B2(N2) (Müller et al. 2016), and 27 sources in the Perseus cloud from PEACHES (Yang et al. 2021).

2019), IRAS 16293-2422 A (hereafter IRAS 16293A; Manigand et al. 2020), IRAS 16293-2422 B (hereafter IRAS 16293B; Jørgensen et al. 2018), and Ser-emb 1, 8, and 17 (Bergner et al. 2019), and a high-mass hot core source Sgr B2(N2) (Belloche et al. 2016; Müller et al. 2016), all observed with ALMA. Note that [CH_3OH] in the case of L483 is inferred from [$^{13}CH_3OH$] assuming $^{12}C/^{13}C = 68$ (Jacobsen et al. 2019), and in the case of IRAS 16293B is calculated based on [$CH_3\,^{18}OH$] assuming $^{16}O/^{18}O = 560$ (Jørgensen et al. 2018). Applying $^{12}C/^{13}C = 50$ (Kahane et al. 2018), the D/H ratio of methanol in the ALMASOP hot corinos is overall consistent with the literature. The D/H ratios in the hot corino sources are an order of magnitude higher than that in Sgr B2(N2), as is found by Taquet et al. (2019).

5.3.2. Complex Organic Molecules

We explore possible correlations between the column densities of CH_3OH, CH_3CHO, $HCOOCH_3$, and C_2H_5OH in Figure 7 and fit the observed positive correlation trend by a linear proportional function. Possibly resulting from the opacity of CH_3OH, the ratios of [CH_3CHO]/[CH_3OH], [$HCOOCH_3$]/[CH_3OH], and [C_2H_5OH]/[CH_3OH] in our sources (gray squares in Figure 7) are higher than those of the individual sources from the literature derived from the rare isotopologues of methanol rather than the main one. Assuming $^{12}C/^{13}C = 50$ (Kahane et al. 2018), the column density ratios of CH_3CHO, $HCOOCH_3$, and C_2H_5OH with respect to those of (rescaled) CH_3OH in our study, which are, respectively, 0.20%, 1.9%, and 2.9% (black markers in Figure 7), become comparable to the value of the above individual sources.

van Gelder et al. (2020) compared the relative abundance of O-bearing COMs with respect to CH_3OH for star-forming regions in four different clouds (Perseus, Serpens, Ophiuchus, and Orion) and concluded that the abundance ratios of most O-bearing COMs (e.g., $HCOOCH_3$) are similar among different clouds while some COMs (e.g., CH_3CHO and C_2H_5OH) are not. The former may form at an earlier evolutionary stage (i.e., cold prestellar phase), and the latter are more affected by the individual local properties. We compare our results with the literature by using the other isotopologues of methanol rather than the main one. The ratio of [$HCOOCH_3$]/[CH_3OH] appears to be similar while that of [CH_3CHO]/[CH_3OH] is different. This disparity agrees with what van Gelder et al. (2020) suggested. The small number (two) of C_2H_5OH sources in our sample prevents us from examining the diversity in [C_2H_5OH]/[CH_3OH] ratios indicated by van Gelder et al. (2020).

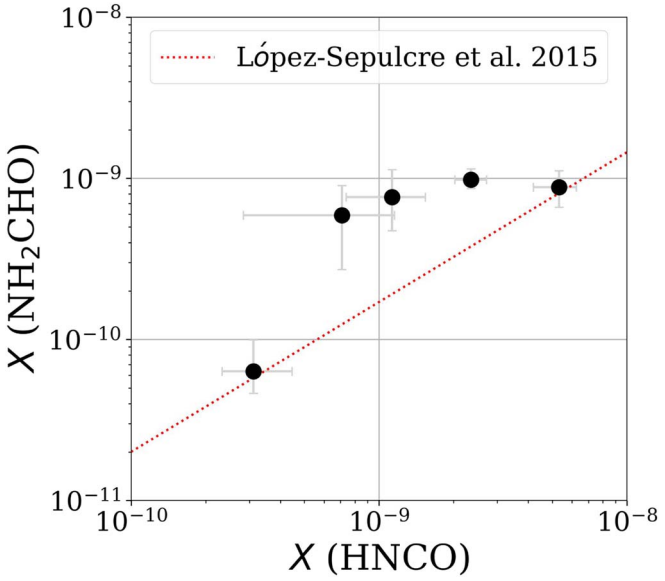

Figure 8. Fractional abundance of NH_2CHO vs. that of HNCO. The red dashed line represents the empirical correlation inferred by López-Sepulcre et al. (2015).

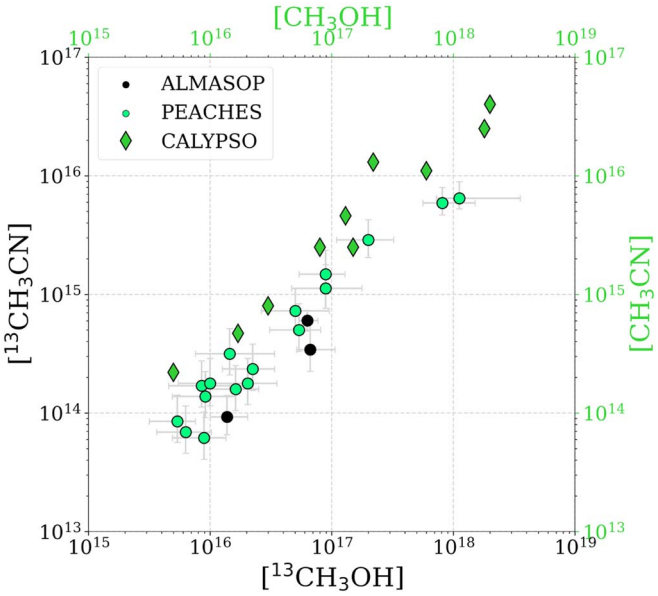

Figure 9. Column densities of methyl cyanide vs. that of methanol in ALMASOP (black circles), PEACHES (green circles; Yang et al. 2021), and CALYPSO (green diamonds; Belloche et al. 2020). Note that this study uses $^{13}CH_3CN$ and $^{13}CH_3OH$ for ALMASOP, and Yang et al. (2021) and Belloche et al. (2020) use CH_3CN and CH_3OH for PEACHES and CALYPSO, respectively.

Using the main isotopologue of methanol (CH_3OH), we also compare our results with the column densities of the corresponding species in the Perseus protostars from PEACHES (Yang et al. 2021) and the three Serpens hot corinos from Bergner et al. (2019). As shown by the gray dashed lines in Figure 7, the column density ratios of CH_3CHO, $HCOOCH_3$, and C_2H_5OH with respect to CH_3OH are generally consistent. This suggests a comparable and non-negligible CH_3OH opacity among these sources.

5.3.3. Prebiotic Molecule

Formamide (NH_2CHO) is one of the main components in both (pre)genetic and (pre)metabolic processes, which makes it a potential key species in prebiotic evolution (Saladino et al. 2012; López-Sepulcre et al. 2019). There are indications that NH_2CHO is chemically related to HNCO. For example, López-Sepulcre et al. (2015) found a tight empirical correlation between their fractional abundances, $X(NH_2CHO) = 0.04 \times X(HNCO)^{0.93}$, in star-forming regions with H_2CO detection. On the one hand, Coutens et al. (2016) came across a comparable D/H ratio of NH_2CHO and HNCO toward IRAS 16293B, suggesting that NH_2CHO and HNCO are chemically related through grain-surface formation. On the other hand, Quénard et al. (2018) demonstrated that the correlation between HNCO and NH_2CHO may originate from their similar response to temperature instead of a chemical link.

Our five sources in which NH_2CHO is detected all bear HNCO, too. Their fractional abundances appear positively correlated, although the NH_2CHO fractional abundances often appear lying above the empirical correlation (See Figure 8). For G211S, the only object where NH_2CHO and HNCO were detected both in the ACA data and the combined data, $X(NH_2CHO)$ is, respectively, 1.9 and 2.5 times higher than the value predicted by the empirical formula, which was based on observations conducted with the Institute for Radio Astronomy in the Millimeter Range 30 m single dish telescope at a lower angular resolution. The disparity we find in higher angular resolution interferometric observations may hint that the spatial distribution of NH_2CHO may be slightly more concentrated at smaller scales.

5.3.4. CH_3CN versus CH_3OH

Yang et al. (2021) found a tight abundance correlation between CH_3CN and CH_3OH in PEACHES. Both Bergner et al. (2017) and Belloche et al. (2020) have shown a similar relation. Here we examine this abundance correlation among the hot corino sources in ALMASOP. Since there is no CH_3CN transition within our spectral coverage, to circumvent the potential optical depth issue of CH_3OH, we consider the column densities of their ^{13}C isotopologues, namely $^{13}CH_3CN$ and $^{13}CH_3OH$. Despite the small number of data points, as shown in Figure 9, the trend of our observational result agrees with Yang et al. (2021). Since the CH_3OH in PEACHES is likely optically thick (see Section 5.3.2), this suggests a high opacity of CH_3CN as well (IRAS 16293 A and B; Calcutt et al. 2018) assuming a consistent trend between ALMASOP and PEACHES.

Figure 9 also shows the data points in the CALYPSO survey (Belloche et al. 2020). The trends of the three data sets (i.e., this study, PEACHES, and CALYPSO) are similar but with small offsets. If the correlation between methanol and methyl cyanide is tight and consistent among different molecular clouds, the offsets may hint at an underlying influence of the opacity to the corresponding molecules.

Based on the tight correlation, Yang et al. (2021) speculated that there is either a common abundance ratio between these two molecules on the icy grains or a common elemental abundance ratio between O and N in the Perseus cloud. As pointed out by Belloche et al. (2020), however, CH_3CN is unlikely chemically linked to CH_3OH since there is no convincing chemical relation between their formation in star-forming regions. In addition, Coutens et al. (2020) modeled the chemical evolution from the prestellar phase to

the formation of the disk and showed that a significant number of species, including CH_3OH and CH_3CN, have similar initial and final abundances. The similarity suggests that these molecules are less sensitive to the history of the physical conditions from the cold core to the disk formation.

6. Conclusion

1. We report the detection of 11 Class 0/I hot corino sources, which harbor compact, warm, and abundant CH_3OH as well as other COMs based on the combined data (TM1+TM2+ACA) of ALMASOP. Four of them were previously identified as hot corino sources with the ALMASOP ACA data.
2. The classification of the only Class I hot corino object in our sample, G208E, may have been based on its high but uncertain bolometric temperature. The reasons for this are: (1) its lack of photometric data at the [70–160] μm bands; (2) its photometric fluxes at other bands are well within the range spanned by Class 0 hot corinos; and (3) the tentative slope of its SED at the near-IR band is similar to Class 0 hot corinos. All of the hot corinos we detect are therefore likely Class 0 protostellar cores.
3. We present the YSO models of the hot corino sources inferred from SED fitting. The SED data points include the photometric data points at 1.3 mm observed by ALMASOP combined data and ACA data in addition to the archival photometric measurements. The sizes of the warm regions (i.e., $T > 100$ K), where the thermal desorption of icy mantles may occur, positively correlate with the observed extent of COMs with a ratio on the order of unity.
4. The bolometric luminosity positively correlates with the extent and the total number of gas-phase methanol. Both of these correlations are consistent with the thermal desorption paradigm for hot corinos.
5. The detection rate of hot corinos may reflect the sensitivities of the underlying observations. The combined data of ALMASOP results in an increased detection rate of hot corinos from 8% in the ACA-only data (Hsu et al. 2020) to 20% in this work. We may find lower-luminosity sources harboring COMs with higher sensitivity observations.
6. The detection rate of warm methanol toward the Orion cloud obtained from this study (ALMASOP) is smaller than that toward the Perseus cloud studied by PEACHES. The distance difference between the two clouds may contribute to the difference while the two rates are statistically similar due to the limited sample size. Observing the same set of COM transitions would enable a fair comparison between cloud properties.
7. As is found in much of the literature on hot corinos, the $^{12}C/^{13}C$ ratio of methanol indicates the high opacity of the main isotopologue (CH_3OH). Assuming $^{12}C/^{13}C = 50$, the fractional column densities of CH_3CHO, $HCOOCH_3$, C_2H_5OH, and CH_2DOH with respect to (rescaled) CH_3OH are 0.019, 0.02, 0.029, and 0.035, respectively. Together with the data toward the hot corinos, the ratio of $[CH_3CHO]/[CH_3OH]$ seems to be more diverse than that of $[HCOOCH_3]/[CH_3OH]$.
8. The ratio of $[^{13}CH_3CN]/[^{13}CH_3OH]$ agrees with the empirical correlation for $[CH_3CN]/[CH_3OH]$ based on the literature, while there is still no clear chemical connection between these two molecules. The three data sets (i.e., ALMASOP, PEACHES, and CALYPSO) of methanol and methyl cyanide exhibit similar trends with small offsets. Assuming the existence of a tight and consistent correlation between methanol and methyl cyanide among different clouds, the offsets may hint at the influence of opacity to the corresponding molecules.

This paper makes use of the following ALMA data: ADS/JAO.ALMA#2018.1.00302.S. ALMA is a partnership of ESO (representing its member states), NSF (USA) and NINS (Japan), together with NRC (Canada), MOST and ASIAA (Taiwan), and KASI (Republic of Korea), in cooperation with the Republic of Chile. The Joint ALMA Observatory is operated by ESO, AUI/NRAO, and NAOJ. S.Y.H. and S.Y.L. acknowledge support from the Ministry of Science and Technology (MoST) with grants 110-2112-M-001-056- and 109-2112-M-001-026-. T.L. acknowledges support by National Natural Science Foundation of China (NSFC) through grant Nos. 12073061 and 12122307, the international partnership program of Chinese Academy of Sciences through grant No. 114231KYSB20200009, and Shanghai Pujiang Program 20PJ1415500. N.H. acknowledges a grant from the Ministry of Science and Technology (MoST) of Taiwan (MoST109-2112-M-001-023- and MoST 110-2112-M-001-048-). Y.-L.Y. acknowledges support from the Virginia Initiative of Cosmic Origins (VICO) Postdoctoral Fellowship. D.J. is supported by the National Research Council of Canada and by an NSERC Discovery Grant. L.B. gratefully acknowledges support from ANID BASAL project FB210003. S.L.Q. is supported by the National Natural Science Foundation of China under grant No. 12033005. C.W.L. is supported by the Basic Science Research Program through the National Research Foundation of Korea (NRF) funded by the Ministry of Education, Science and Technology (NRF-2019R1A2C1010851). P.S. was partially supported by a Grant-in-Aid for Scientific Research (KAKENHI Number 18H01259) of the Japan Society for the Promotion of Science (JSPS). K.T. was supported by JSPS KAKENHI (Grant Number 20H05645). Y.-L. Y. benefited from discussions held with the international team #461 `Provenances of our Solar System's Relics' (team leaders M. N. Drozdovskaya and C. Opitom) at the International Space Science Institute (ISSI), Bern, Switzerland. A.S. was supported by National Science Foundation under grant AST-1715876. J.-E. Lee is supported by the National Research Foundation of Korea (NRF) grant funded by the Korea government (MSIT) (grant number 2021R1A2C1011718). J.J.Z was supported by the National Natural Science foundation of China (NSFC) under grant No. 11973076. This research made use of Astropy,[27] a community-developed core Python package for Astronomy (Astropy Collaboration et al. 2013; Price-Whelan et al. 2018).

Software: astropy (Astropy Collaboration et al. 2013; Price-Whelan et al. 2018), CASA (McMullin et al. 2007), HOCHUNK (Whitney et al. 2003) SED Fitter (Robitaille et al. 2006, 2007) XCLASS (Möller et al. 2017).

[27] http://www.astropy.org

Appendix A
Source Overview

A.1. Literature Review

There are seven HOPS objects (Furlan et al. 2016) in the 11 hot corinos. Six of them are included in the Very Large Array (VLA)/ALMA Nascent Disk and Multiplicity (VANDAM) Survey of Orion Protostars (Tobin et al. 2020). Four of them are included in the Combined Array for Research in Millimeter Astronomy - Nobeyama Radio Observatory (CARMA-NRO) Orion Survey (Kong et al. 2018; Feddersen et al. 2020). Table A1 lists the surveys and the related sources.

Not all of the 11 hot corino sources are known or bright YSOs. Here we summarize the literature related to 11 sources individually:

1. *G192.12–11.10 (G192)*: First detected as a hot corino in the ACA data of ALMASOP (Hsu et al. 2020). Yi et al. (2018) reported it as a starless core. Individual studies for this source are rare.
2. *G196.92–10.37–A (G196A)*: G196A was identified as a YSO candidate in Dunham et al. (2008) based on the Spitzer Space Telescope Legacy Project, "From Molecular Cores to Planet Forming Disks" (Evans et al. 2003).
3. *G203.21–11.20W2 (G203W2)*: There are not many studies toward this source, even though it is in the Orion B cloud. It is not within the spatial coverage of the HOPS catalog.
4. *G205.46–14.56S1–A (G205S1A)*: This source shows apparent CO $J = 1 - 0$, $J = 4 - 3$, and $J = 3 - 2$ outflow, which are suspected to contaminate the field of HOPS–401 (Nagy et al. 2020). In addition, G205S1A showed a declining light curve in 850 μm for 16 months in the JCMT Transient Survey (Mairs et al. 2018). Lee et al. (2021), with a 4 yr summary of the survey, further reported a linearly declining light curve for this source.
5. *G206.93–16.61W2 (G206W2)*: Similar to G205S1A, the apparent CO $J = 1 - 0$, $J = 4 - 3$, and $J = 3 - 2$ outflow is suspected to contaminate the field of HOPS–272 (Nagy et al. 2020).
6. *G208.68–19.20N1 (G208N1)*: First detected as a hot corino in the ACA data of ALMASOP (Hsu et al. 2020). G208N1, coinciding with OMC3/MMS6, has a very young outflow, indicating that this source is at its very earliest stage of evolution (Chini et al. 1997; Takahashi & Ho 2012; Takahashi et al. 2019).
7. *G208.89–20.04E (G208E)*: This source is one of the targets in Megeath et al. (2012) but not included in the HOPS catalog due to the lack of 24 μm detection.
8. *G209.55–19.68N1-B (G209N1B)*: The CARMA-NRO Orion Survey (Kong et al. 2018) reported a clear blue lobe of the CO outflow in G209N1B. Although the outflow is not obvious in its CO $J = 2 - 1$ moment-0 image (Figure C2), the large line width of the CO $J = 2 - 1$ transition implies the existence of the outflow.
9. *G209.55–19.68S1 (G209S1)*: G209S1 has been involved in a survey of companions around YSOs conducted with the Hubble Space Telescope by Kounkel et al. (2016), who reported that the companion fraction in the high stellar density region is higher than that in the low stellar density region.
10. *G210.49–19.79W–A (G210WA)*: First detected as a hot corino in the ACA data of ALMASOP (Hsu et al. 2020). This source is associated with HH 1–2 VLA 3, which is reported to be in an active state of mass infall and accretion (Fischer et al. 2010). It also coincides to the CH_3OH maser KLC–2 (e.g., Lo et al. 1975; Kang et al.2013).
11. *G211.47–19.27S (G211S)*: First detected as a hot corino in the ACA data of ALMASOP (Hsu et al. 2020). This is the most line-rich source, which meanwhile has the highest luminosity, among the 11 hot corinos reported in this study.

Table A1
Surveys Related to the Sources

	HOPS	VANDAM	CARMA-NRO
G192			
G196A			
G203W2			
G205S1A	358		
G206W2	399	V	
G208N1	87	V	V
G208E			
G209N1B	12	V	V
G209S1	11	V	V
G210WA	168	V	V
G211S	288	V	

References. HOPS: Furlan et al. (2016); VANDAM Survey of Orion Protostars: Tobin et al. (2020); CARMA-NRO Orion Survey: Kong et al. (2018); Feddersen et al. (2020).

Table A2
Results of 2D Gaussian Fitting

Name	HPBW (″)	Source Size (CH_3OH) (″)	$N(H_2)$ (cm^{-2})
G192	0.41	0.35 ± 0.03	2.1×10^{24}
G196A	0.44	0.36 ± 0.07	4.3×10^{23}
G203W2	0.43	0.23 ± 0.05	1.9×10^{23}
G205S1A	0.43	0.41 ± 0.01	1.2×10^{24}
G206W2	0.41	0.31 ± 0.08	4.7×10^{24}
G208N1	0.41	0.64 ± 0.03	8.2×10^{24}
G208E	0.42	0.28 ± 0.04	5.8×10^{23}
G209N1B	0.42	0.33 ± 0.03	5.0×10^{23}
G209S1	0.41	0.45 ± 0.07	1.7×10^{24}
G210WA	0.42	0.37 ± 0.01	1.5×10^{24}
G211S	0.46	0.64 ± 0.04	3.5×10^{24}

Note. HPBW is the half-power beam width of the synthesized beam. The source size is the geometric mean of the FWHM sizes along the major and the minor axes of the deconvolved CH_3OH–46 moment-0 image. N_{H_2} is the column density of molecular hydrogen within the source size over which the dust temperature is assumed to be 100 K. See Hsu et al. (2020) for the formula and the parameters.

A.2. 2D Gaussian Fitting

Based on the 2D Gaussian fitting in CASA to the CH_3OH–46K transition moment-0 images, we infer the extent of the methanol emission and calculate the molecular hydrogen column density $N(H_2)$ using the 1.3 continuum flux within the extent. We use the formulae in Hsu et al. (2020) and Kauffmann et al. (2008) for optically thin continuum emission. The dust opacity is in the form of $\kappa_\nu = 0.1(\nu/1\ \mathrm{THz})^\beta \mathrm{cm}^2\mathrm{g}^{-1}$. The dust opacity index β was assigned to be 1.70, which is a typical value for cold clumps in the submillimeter band

Table A3
Information of Potential Hot Corinos

Name	Cloud	α_{J2000}	δ_{J2000}
G205.46-14.56M2-D	Orion B	05h46m08.43 s	−00d10m00.5 s
G205.46-14.56N2	Orion B	05h46m07.72 s	−00d12m21.27 s
G205.46-14.56S1-B	Orion B	05h46m07.33 s	−00d13m43.49 s
G205.46-14.56S2	Orion B	05h46m04.77 s	−00d14m16.67 s
G208.68-19.20N3-A	Orion A	05h35m18.06 s	−05d00m18.19 s
G208.68-19.20S-A	Orion A	05h35m26.56 s	−05d03m55.11 s
G208.68-19.20S-B	Orion A	05h35m26.54 s	−05d03m55.71 s
G209.55-19.68N1-A	Orion A	05h35m08.95 s	−05d55m54.98 s
G209.55-19.68N1-C	Orion A	05h35m08.57 s	−05d55m54.54s

Note. α_{J2000} and δ_{J2000} are the R.A. and decl., respectively, of the peak position in our combined 1.3 mm continuum observations.

(Beckwith et al. 1990; Juvela et al. 2018). We assumed a (dust) temperature of 100 K, which is the typical value for hot corinos. Table A2 briefly summarizes the 2D Gaussian fitting result of the 1.3 mm continuum images, including the HPBW of the observation, the FWHM of the source angular size, and the integrated flux density. The HPBW is around 0.″45. The deconvolved FWHM ranges from 0.″23 to 0.″64. The column density of molecular hydrogen ranges from 1.5×10^{23} cm^{-2} to 2.2×10^{25} cm^{-2}.

A.3. Potential Hot Corinos

Table A3 shows the list of the potential hot corinos. The potential hot corinos are, following the criteria of PEACHES, the protostellar cores where at least one methanol transition was detected at 3σ. See Section 5.2.3 for more discussions.

Appendix B
Molecular Analysis

B.1. Molecular Parameters of Hot Corino Sources

Tables B1–B11 show the parameters of the molecular components optimized by MAGIX for each source. The parameters T_{ex}, N, δv, and v_{LSR} are the excitation temperature, the total column density, the line width, and the local-standard-of-rest velocity of the component, respectively. To derive the fractional abundance X for each molecular component, please refer to the column density of the molecular hydrogen in Table A2. We fix the emission size of all species to be the (2D Gaussian) extent of the CH_3OH-46K transition deconvolved by the beam size (Table A2). The errors estimated by MAGIX are also presented. The excitation temperature T_{ex} of the species detected with only a single transition are fixed to be 100 K. The CO $J = 2 - 1$ transition is detected in all of the sources but not fitted by XCLASS due to the non-Gaussian line profile.

B.2. Spectra of Hot Corino Sources

Figure set B1 shows all of the spectra of the hot corino sources (see Figure B1 for an example). The red curve is the spectrum exported by XCLASS. The molecules of transitions with their peak brightness temperatures higher than 5σ are labeled. Note that the ranges of both the x- and y-axis of the spectra for each source are different for better illustrations.

B.3. Moment-0 Images in the Hot Corinos

For the 11 hot corinos, Figure B2 shows the moment-0 images of methanol transition:

1. CH_3OH: 231281 MHz; 165 K;

$$\text{rovib} = \text{A2};\ J = 10 - 9;\ K_a = 2 - 3;\ K_c = 9 - 6.$$

The small FWHM, illustrated by the aqua eclipses, implies that the deconvolved source sizes are all compact.

In addition, Figure B3 displays the moment-0 images of selected molecules/transitions in G211S, which is the most line-rich hot corino in our sample. The transitions from panel (a) to (j) are:

(a) CH_3OH: 218440 MHz; 45 K;
rovib=E; $J = 5 - 4$; $K_a = 1 - 2$; $K_c = 4 - 3$;
(b) CH_3OH: 232784 MHz; 447 K;
rovib=A2; $J = 18 - 17$; $K_a = 3 - 4$; $K_c = 15 - 14$;
(c) $^{13}CH_3OH$: 216370 MHz; 162 K;
$J = 10 - 9$; $K_a = 2 - 3$; $K_c = 9 - 6$; rot=A2;
(d) CH_2DOH: 218316 MHz; 59 K;
$J = 5$; $K_a = 2 - 1$; $K_c = 4 - 5$; rot=e1;
(e) CH_3CHO: 216582 MHz; 65 K;
$J = 11 - 10$; $K_a = 1$; $K_c = 10 - 9$; rovib=E;
(f) $HCOOCH_3$: 216966 MHz; 112 K;

$J = 20 - 19$; $K_a = 0/1/0 - 1$; $K_c = 20 - 19$; rovib=E/A;
(g) NH_2CHO: 232274 MHz; 79 K;
$J = 11 - 10$; $K_a = 2$; $K_c = 10 - 9$;
(h) H_2CO: 218222 MHz; 21 K;
$J = 3 - 2$; $K_a = 0$; $K_c = 3 - 2$;
(i) D_2CO: 231410 MHz; 28 K;
$J = 4 - 3$; $K_a = 0$; $K_c = 4 - 3$;
(j) HNCO: 218981 MHz; 101 K;
$J = 10 - 9$; $K_a = 1$; $K_c = 10 - 9$.

B.4. List of Detected Molecules/Transitions

Table B12 shows all of the detected molecular transitions. The data are exported from XCLASS and adapted from Cologne Database for Molecular Spectroscopy (CDMS; Müller et al. 2005) and Jet Propulsion Laboratory (Pickett et al. 1998).

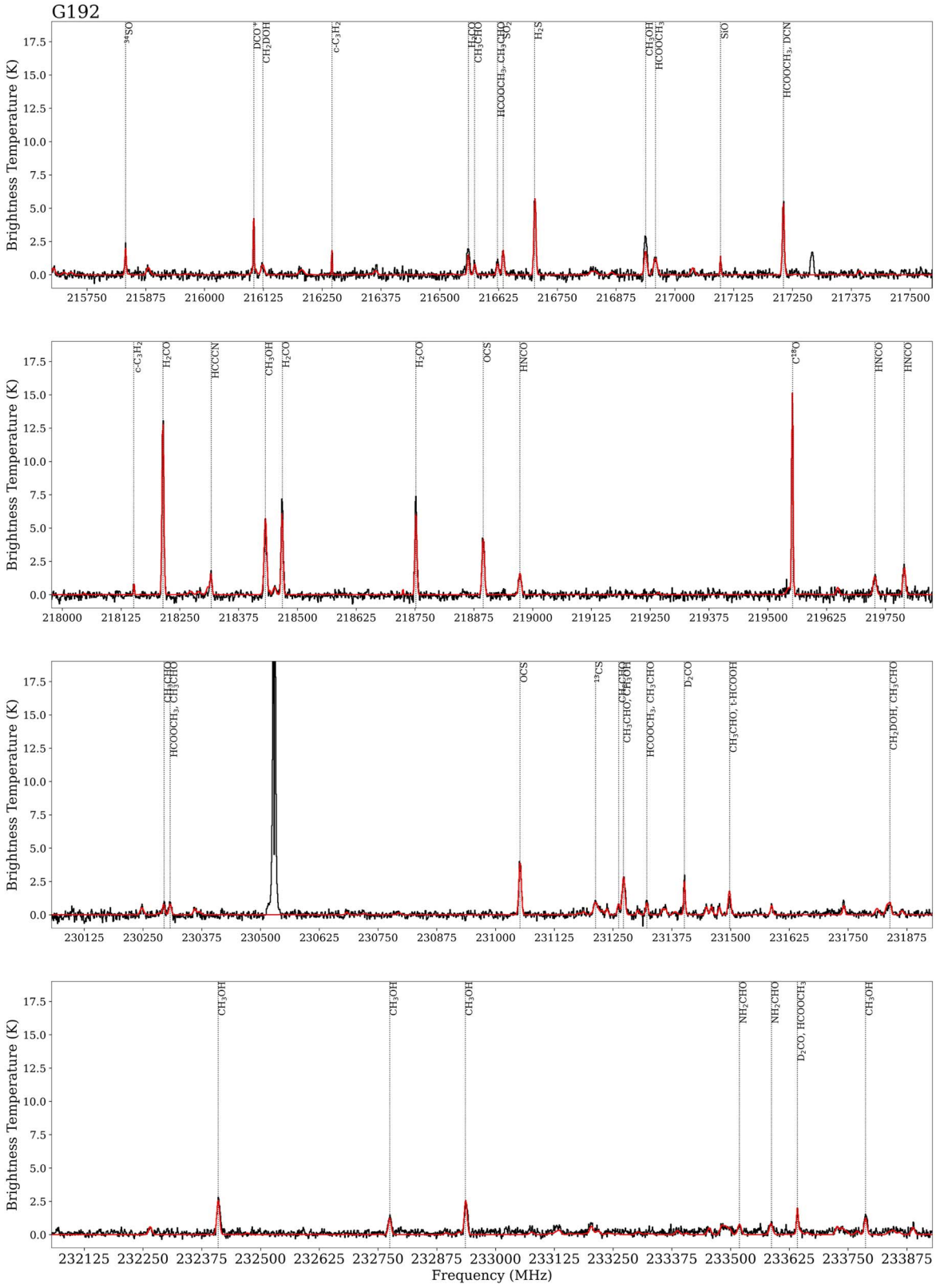

Figure B1. Observed spectrum and the XCLASS simulation result. The complete figure set (15 images) is available.

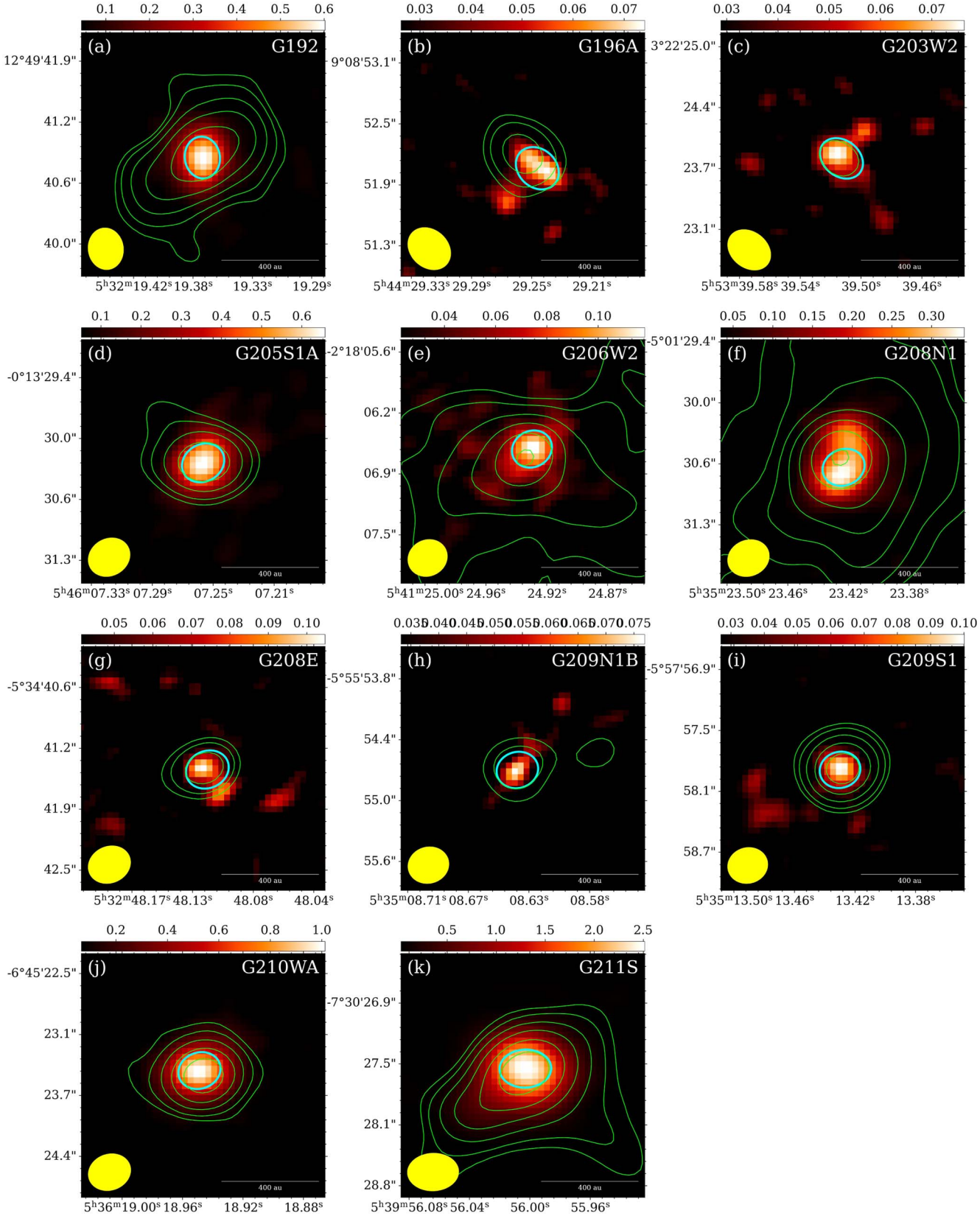

Figure B2. Moment-0 images of the CH_3OH $10_{2,9} - 9_{3,6}$ transition (E_{up}=165 K and f_{rest}=231281 MHz). The green contours show the continuum in steps of [3, 5, 10, 20, 40, 80, 160]σ. The aqua ellipses show the FWHM of the 2D Gaussian fits of the deconvolved methanol emission. The yellow ellipses show the FWHM of the synthesized beam.

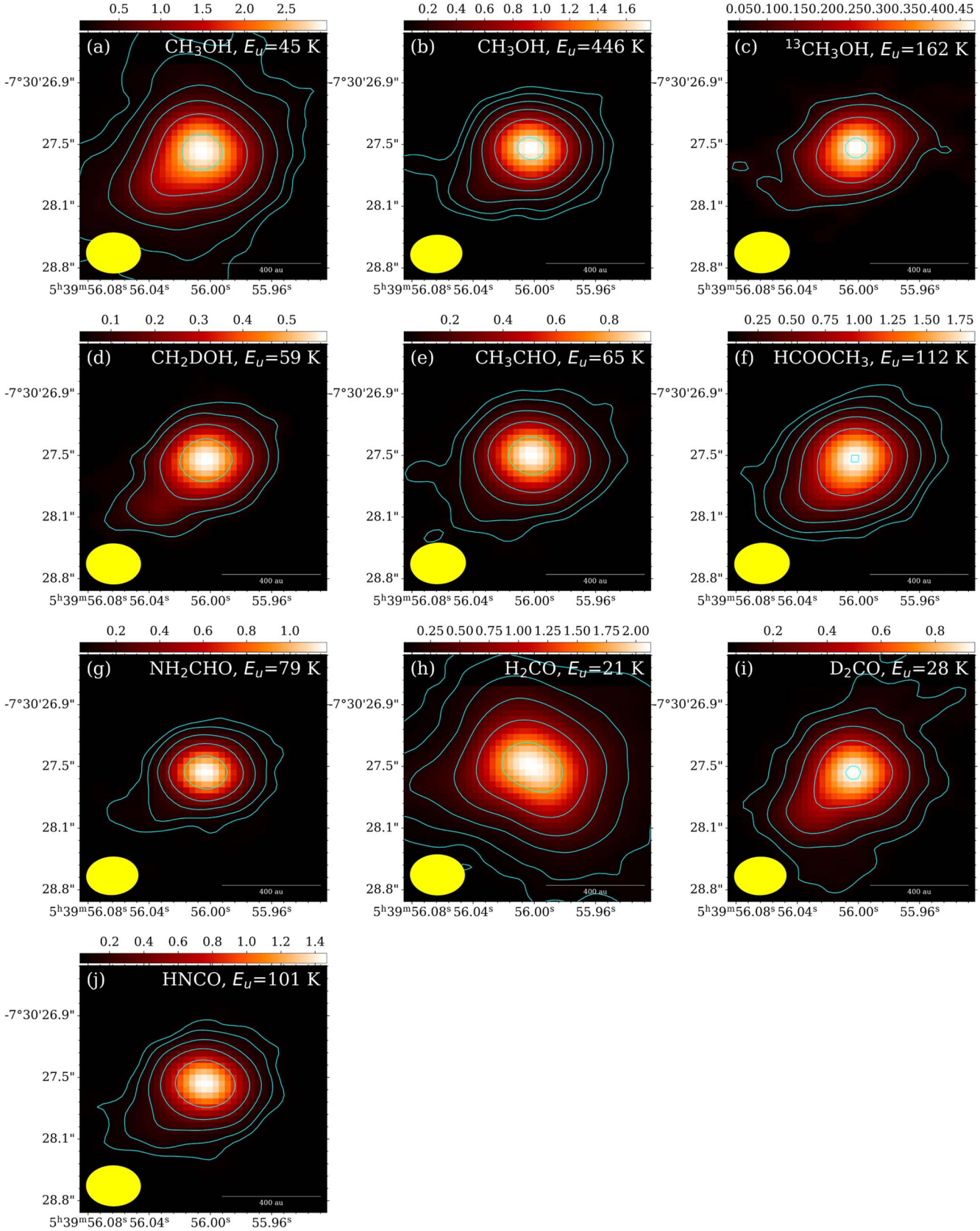

Figure B3. Moment-0 images of G211S. The aqua contours are in steps of [3, 5, 10, 20, 40, 80, 160]σ for each transition. See Appendix B for more information of the transitions. The yellow ellipses show the FWHM of the synthesized beam.

Table B1
Molecular Parameters of G192

Species	T_{ex} (K)	N ($\log_{10}$(cm^{-2}))	δv (km s^{-1})	v_{LSR} (km s^{-1})
CH_3OH;v = 0;	194^{+9}_{-8}	$17.10^{+0.09}_{-0.11}$	$8.9^{+0.7}_{-0.6}$	$10.2^{+0.3}_{-0.4}$
$^{13}CH_3OH$;v = 0;	374^{+11}_{-7}	$16.53^{+0.20}_{-0.20}$	$11.4^{+0.7}_{-0.5}$	$8.0^{+0.3}_{-0.3}$
CH_2DOH;v = 0;	74^{+9}_{-7}	$16.70^{+0.19}_{-0.19}$	$11.0^{+0.7}_{-0.5}$	$7.6^{+0.3}_{-0.3}$
$CH_3\ ^{18}OH$;v = 0;	...	...	...	...
C_2H_5OH;v = 0;	...	...	...	...
CH_3CHO;v = 0;	110^{+9}_{-9}	$15.22^{+0.19}_{-0.15}$	$7.2^{+0.8}_{-0.6}$	$9.4^{+0.3}_{-0.3}$
CH_3CHO;v15 = 1;	...	...	...	...
$HCOOCH_3$;v = 0;	480^{+9}_{-8}	$16.42^{+0.23}_{-0.16}$	$11.6^{+0.9}_{-0.5}$	$9.6^{+0.3}_{-0.4}$
$HCOOCH_3$;v18 = 1;	...	...	...	...
CH_3OCH_3;v = 0;	...	...	...	...
$CH_2(OH)CHO$;v = 0;	...	...	...	...
aGg'-$(CH_2OH)_2$;v = 0;	...	...	...	...
H_2CO;v = 0;	239^{+11}_{-6}	$16.29^{+0.06}_{-0.07}$	$6.3^{+0.7}_{-0.5}$	$10.4^{+0.3}_{-0.2}$
D_2CO;v = 0;	254^{+7}_{-11}	$15.19^{+0.23}_{-0.15}$	$5.0^{+0.8}_{-0.5}$	$9.9^{+0.4}_{-0.2}$
t-HCOOH;v = 0;	(100)	$15.43^{+0.16}_{-0.24}$	$8.1^{+0.6}_{-0.7}$	$10.2^{+0.2}_{-0.4}$
NH_2CHO;v = 0;	395^{+10}_{-7}	$15.22^{+0.17}_{-0.21}$	$10.3^{+0.7}_{-0.7}$	$10.1^{+0.3}_{-0.3}$
HNCO;v = 0;	205^{+7}_{-8}	$15.38^{+0.13}_{-0.19}$	$9.0^{+0.7}_{-0.7}$	$10.1^{+0.4}_{-0.2}$
C_2H_5CN;v = 0;	...	...	...	...
$^{13}CH_3CN$;v = 0;	...	...	...	...
DCN;v = 0;	(100)	$14.21^{+0.14}_{-0.14}$	$6.5^{+0.7}_{-0.6}$	$10.1^{+0.3}_{-0.3}$
HCCCN;v = 0;	(100)	$13.88^{+0.22}_{-0.19}$	$5.5^{+0.7}_{-0.7}$	$10.6^{+0.4}_{-0.2}$
^{13}CS;v = 0;	(100)	$13.98^{+0.25}_{-0.19}$	$10.0^{+0.8}_{-0.4}$	$10.2^{+0.4}_{-0.3}$
H_2S;v = 0;	(100)	$15.89^{+0.10}_{-0.17}$	$6.8^{+0.6}_{-0.6}$	$10.3^{+0.3}_{-0.3}$
OCS;v = 0;	63^{+10}_{-8}	$15.83^{+0.13}_{-0.13}$	$8.0^{+0.7}_{-0.6}$	$10.6^{+0.4}_{-0.3}$
$O^{13}CS$;v = 0;	...	...	...	...
^{34}SO;v = 0;	(100)	$14.65^{+0.24}_{-0.16}$	$4.7^{+0.7}_{-0.6}$	$10.1^{+0.4}_{-0.2}$
SO_2;v = 0;	(100)	$15.90^{+0.15}_{-0.23}$	$6.7^{+0.7}_{-0.6}$	$10.8^{+0.3}_{-0.3}$
CCD;v = 0;	...	...	...	...
c-C_3H_2;v = 0;	27^{+7}_{-8}	$14.18^{+0.29}_{-0.14}$	$2.7^{+0.6}_{-0.7}$	$10.3^{+0.3}_{-0.4}$
DCO^+;v = 0;	(100)	$13.60^{+0.16}_{-0.20}$	$3.5^{+0.7}_{-0.7}$	$10.4^{+0.4}_{-0.3}$
$N2D^+$;v = 0;	...	...	...	...
$C^{18}O$;v = 0;	(100)	$17.40^{+0.09}_{-0.07}$	$4.6^{+0.6}_{-0.5}$	$10.1^{+0.3}_{-0.2}$
SiO;v = 0;	(100)	$13.32^{+0.23}_{-0.19}$	$3.2^{+0.7}_{-0.7}$	$10.0^{+0.3}_{-0.3}$

Table B2
Molecular Parameters of G196A

Species	T_{ex} (K)	N ($\log_{10}$(cm^{-2}))	δv (km s^{-1})	v_{LSR} (km s^{-1})
CH_3OH;v = 0;	190^{+13}_{-24}	$16.57^{+0.33}_{-0.22}$	$9.2^{+1.4}_{-1.2}$	$9.4^{+0.6}_{-0.8}$
$^{13}CH_3OH$;v = 0;	...	...	...	...
CH_2DOH;v = 0;	...	...	...	...
$CH_3\ ^{18}OH$;v = 0;	...	...	...	...
C_2H_5OH;v = 0;	...	...	...	...
CH_3CHO;v = 0;	...	...	...	...
CH_3CHO;v15 = 1;	...	...	...	...
$HCOOCH_3$;v = 0;	...	...	...	...
$HCOOCH_3$;v18 = 1;	...	...	...	...
CH_3OCH_3;v = 0;	...	...	...	...
$CH_2(OH)CHO$;v = 0;	...	...	...	...
aGg'-$(CH_2OH)_2$;v = 0;	...	...	...	...
H_2CO;v = 0;	175^{+19}_{-13}	$15.74^{+0.11}_{-0.21}$	$4.6^{+1.3}_{-1.1}$	$10.3^{+0.5}_{-0.5}$
D_2CO;v = 0;	...	...	...	...
t-HCOOH;v = 0;	...	...	...	...
NH_2CHO;v = 0;	...	...	...	...
HNCO;v = 0;	...	...	...	...
C_2H_5CN;v = 0;	...	...	...	...
$^{13}CH_3CN$;v = 0;	...	...	...	...

Table B2
(Continued)

Species	T_{ex} (K)	N ($\log_{10}$(cm^{-2}))	δv (km s^{-1})	v_{LSR} (km s^{-1})
DCN;v = 0;	(100)	$13.73^{+0.36}_{-0.31}$	$5.1^{+1.3}_{-1.1}$	$10.9^{+0.8}_{-0.5}$
HCCCN;v = 0;	(100)	$13.78^{+0.28}_{-0.52}$	$4.7^{+1.5}_{-1.2}$	$11.3^{+0.9}_{-0.6}$
^{13}CS;v = 0;	(100)	$13.60^{+0.40}_{-0.40}$	$5.9^{+1.5}_{-1.5}$	$10.3^{+0.6}_{-0.6}$
H_2S;v = 0;	(100)	$15.32^{+0.28}_{-0.46}$	$7.6^{+1.2}_{-1.6}$	$10.9^{+0.6}_{-0.8}$
OCS;v = 0;	303^{+16}_{-18}	$15.42^{+0.33}_{-0.38}$	$10.5^{+1.4}_{-1.4}$	$12.1^{+0.8}_{-0.6}$
$O^{13}CS$;v = 0;	...	...	...	...
^{34}SO;v = 0;	(100)	$14.29^{+0.39}_{-0.38}$	$4.5^{+1.6}_{-1.2}$	$10.6^{+0.6}_{-0.7}$
SO_2;v = 0;	(100)	$15.82^{+0.41}_{-0.43}$	$14.4^{+1.5}_{-1.5}$	$12.4^{+0.6}_{-0.7}$
CCD;v = 0;	104^{+21}_{-14}	$14.68^{+0.27}_{-0.51}$	$3.1^{+1.2}_{-1.5}$	$10.8^{+0.8}_{-0.5}$
c-C_3H_2;v = 0;	24^{+18}_{-12}	$14.41^{+0.31}_{-0.46}$	$2.4^{+1.3}_{-1.3}$	$11.1^{+0.5}_{-0.7}$
DCO^+;v = 0;	(100)	$13.29^{+0.34}_{-0.42}$	$2.9^{+1.1}_{-1.7}$	$10.8^{+0.6}_{-0.6}$
$N2D^+$;v = 0;	...	...	...	...
$C^{18}O$;v = 0;	(100)	$17.07^{+0.10}_{-0.19}$	$3.0^{+1.0}_{-1.0}$	$10.8^{+0.5}_{-0.3}$
SiO;v = 0;	(100)	$13.35^{+0.29}_{-0.55}$	$4.2^{+1.2}_{-1.5}$	$10.5^{+0.6}_{-0.8}$

Table B3
Molecular Parameters of G203W2

Species	T_{ex} (K)	N ($\log_{10}$(cm^{-2}))	δv (km s^{-1})	v_{LSR} (km s^{-1})
CH_3OH;v = 0;	229^{+12}_{-18}	$16.82^{+0.23}_{-0.42}$	$6.7^{+1.6}_{-1.1}$	$9.3^{+0.7}_{-0.6}$
$^{13}CH_3OH$;v = 0;	...	...	...	...
CH_2DOH;v = 0;	...	...	...	...
$CH_3\ ^{18}OH$;v = 0;	...	...	...	...
C_2H_5OH;v = 0;	...	...	...	...
CH_3CHO;v = 0;	...	...	...	...
CH_3CHO;v15 = 1;	...	...	...	...
$HCOOCH_3$;v = 0;	...	...	...	...
$HCOOCH_3$;v18 = 1;	...	...	...	...
CH_3OCH_3;v = 0;	...	...	...	...
$CH_2(OH)CHO$;v = 0;	...	...	...	...
aGg'-$(CH_2OH)_2$;v = 0;	...	...	...	...
H_2CO;v = 0;	186^{+20}_{-13}	$15.85^{+0.19}_{-0.19}$	$3.0^{+1.7}_{-0.9}$	$9.6^{+0.5}_{-0.6}$
D_2CO;v = 0;	29^{+13}_{-20}	$14.24^{+0.44}_{-0.29}$	$3.0^{+1.8}_{-1.2}$	$9.7^{+0.7}_{-0.7}$
t-HCOOH;v = 0;	...	...	...	...
NH_2CHO;v = 0;	...	...	...	...
HNCO;v = 0;	323^{+14}_{-17}	$15.30^{+0.32}_{-0.39}$	$5.9^{+1.3}_{-1.3}$	$9.3^{+0.5}_{-0.8}$
C_2H_5CN;v = 0;	...	...	...	...
$^{13}CH_3CN$;v = 0;	...	...	...	...
DCN;v = 0;	(100)	$13.92^{+0.26}_{-0.49}$	$2.7^{+1.3}_{-1.3}$	$9.9^{+0.7}_{-0.7}$
HCCCN;v = 0;	(100)	$13.88^{+0.49}_{-0.38}$	$3.8^{+1.0}_{-1.6}$	$9.1^{+0.9}_{-0.7}$
^{13}CS;v = 0;	...	...	...	...
H_2S;v = 0;	(100)	$15.39^{+0.35}_{-0.43}$	$3.4^{+1.2}_{-1.3}$	$9.0^{+0.7}_{-0.7}$
OCS;v = 0;	273^{+25}_{-11}	$15.65^{+0.35}_{-0.35}$	$5.6^{+1.7}_{-1.2}$	$9.9^{+0.6}_{-0.8}$
$O^{13}CS$;v = 0;	...	...	...	...
^{34}SO;v = 0;	...	...	...	...
SO_2;v = 0;	...	...	...	...
CCD;v = 0;	...	...	...	...
c-C_3H_2;v = 0;	...	...	...	...
DCO^+;v = 0;	(100)	$13.76^{+0.38}_{-0.33}$	$1.2^{+0.9}_{-0.7}$	$9.8^{+0.7}_{-0.5}$
$N2D^+$;v = 0;	(100)	$13.22^{+0.46}_{-0.38}$	$0.5^{+0.4}_{-0.3}$	$10.0^{+0.7}_{-0.5}$
$C^{18}O$;v = 0;	(100)	$17.14^{+0.23}_{-0.25}$	$2.0^{+1.4}_{-0.9}$	$9.6^{+0.6}_{-0.5}$
SiO;v = 0;_1	(100)	$14.13^{+0.31}_{-0.38}$	$14.5^{+1.7}_{-1.1}$	$6.8^{+0.8}_{-0.6}$
SiO;v = 0;_2	(100)	$14.47^{+0.20}_{-0.34}$	$18.2^{+1.5}_{-1.3}$	$-11.9^{+23.3}_{-24.7}$

Table B4
Molecular Parameters of G205S1A

Species	T_{ex} (K)	N ($\log_{10}(cm^{-2})$)	δv (km s^{-1})	v_{LSR} (km s^{-1})
$CH_3OH;v=0$;	142^{+9}_{-7}	$17.02^{+0.06}_{-0.11}$	$8.3^{+0.7}_{-0.6}$	$10.4^{+0.3}_{-0.3}$
$^{13}CH_3OH;v=0$;	207^{+8}_{-8}	$16.82^{+0.21}_{-0.11}$	$15.8^{+0.8}_{-0.5}$	$8.5^{+0.3}_{-0.3}$
$CH_2DOH;v=0$;	87^{+8}_{-8}	$16.92^{+0.11}_{-0.20}$	$14.8^{+0.6}_{-0.6}$	$9.8^{+0.4}_{-0.3}$
$CH_3\ ^{18}OH;v=0$;	...	...	...	...
$C_2H_5OH;v=0$;	...	...	...	...
$CH_3CHO;v=0$;	163^{+8}_{-8}	$15.67^{+0.17}_{-0.14}$	$15.1^{+0.7}_{-0.7}$	$11.0^{+0.4}_{-0.3}$
$CH_3CHO;v15=1$;	...	...	...	...
$HCOOCH_3;v=0$;	399^{+8}_{-8}	$16.75^{+0.12}_{-0.14}$	$13.2^{+0.6}_{-0.8}$	$10.4^{+0.4}_{-0.2}$
$HCOOCH_3;v18=1$;	...	...	...	...
$CH_3OCH_3;v=0$;	295^{+8}_{-8}	$16.51^{+0.17}_{-0.17}$	$12.2^{+0.7}_{-0.5}$	$9.9^{+0.4}_{-0.3}$
$CH_2(OH)CHO;v=0$;	...	...	...	...
aGg'-$(CH_2OH)_2;v=0$;	...	...	...	...
$H_2CO;v=0$;	276^{+10}_{-6}	$16.54^{+0.04}_{-0.07}$	$7.8^{+0.8}_{-0.3}$	$10.5^{+0.3}_{-0.3}$
$D_2CO;v=0$;	344^{+9}_{-8}	$15.39^{+0.19}_{-0.19}$	$8.3^{+0.6}_{-0.6}$	$10.6^{+0.3}_{-0.4}$
t-HCOOH;v = 0;	...	...	...	...
$NH_2CHO;v=0$;	...	...	...	...
$HNCO;v=0$;	119^{+9}_{-7}	$15.30^{+0.17}_{-0.14}$	$13.0^{+0.9}_{-0.6}$	$9.9^{+0.4}_{-0.4}$
$C_2H_5CN;v=0$;	...	...	...	...
$^{13}CH_3CN;v=0$;	427^{+7}_{-9}	$14.53^{+0.22}_{-0.18}$	$10.4^{+0.6}_{-0.6}$	$11.4^{+0.4}_{-0.3}$
$DCN;v=0$;	(100)	$14.32^{+0.12}_{-0.14}$	$8.4^{+0.7}_{-0.7}$	$10.2^{+0.3}_{-0.3}$
$HCCCN;v=0$;	(100)	$14.54^{+0.14}_{-0.17}$	$9.5^{+0.5}_{-0.8}$	$10.8^{+0.3}_{-0.3}$
$^{13}CS;v=0$;	(100)	$14.28^{+0.19}_{-0.19}$	$12.3^{+0.6}_{-0.8}$	$9.5^{+0.3}_{-0.4}$
$H_2S;v=0$;	(100)	$15.90^{+0.15}_{-0.12}$	$7.9^{+0.6}_{-0.8}$	$10.2^{+0.4}_{-0.3}$
$OCS;v=0$;	65^{+9}_{-6}	$15.95^{+0.09}_{-0.14}$	$9.6^{+0.7}_{-0.7}$	$10.4^{+0.4}_{-0.3}$
$O^{13}CS;v=0$;	407^{+8}_{-9}	$15.23^{+0.24}_{-0.22}$	$9.4^{+0.7}_{-0.8}$	$12.5^{+0.4}_{-0.3}$
$^{34}SO;v=0$;	(100)	$14.90^{+0.20}_{-0.20}$	$16.9^{+0.8}_{-0.4}$	$9.7^{+0.3}_{-0.3}$
$SO_2;v=0$;	(100)	$16.07^{+0.22}_{-0.18}$	$15.5^{+0.6}_{-0.7}$	$12.4^{+0.4}_{-0.3}$
CCD;v = 0;	...	...	...	...
c-$C_3H_2;v=0$;	...	...	...	...
$DCO^+;v=0$;	(100)	$13.63^{+0.16}_{-0.20}$	$4.9^{+0.6}_{-0.6}$	$10.7^{+0.4}_{-0.3}$
$N2D^+;v=0$;	...	...	...	...
$C^{18}O;v=0$;	(100)	$17.05^{+0.14}_{-0.13}$	$4.4^{+0.8}_{-0.5}$	$10.3^{+0.4}_{-0.3}$
SiO;v = 0;_1	(100)	$13.36^{+0.17}_{-0.26}$	$8.6^{+0.6}_{-0.6}$	$24.3^{+0.3}_{-0.4}$
SiO;v = 0;_2	(100)	$13.62^{+0.27}_{-0.18}$	$12.5^{+0.6}_{-0.7}$	$1.9^{+0.3}_{-0.3}$

Table B5
Molecular Parameters of G206W2

Species	T_{ex} (K)	N ($\log_{10}(cm^{-2})$)	δv (km s^{-1})	v_{LSR} (km s^{-1})
$CH_3OH;v=0$;	349^{+10}_{-8}	$16.90^{+0.21}_{-0.17}$	$3.1^{+0.8}_{-0.7}$	$8.9^{+0.5}_{-0.3}$
$^{13}CH_3OH;v=0$;	...	...	...	...
$CH_2DOH;v=0$;	78^{+8}_{-10}	$16.75^{+0.21}_{-0.21}$	$7.8^{+0.9}_{-0.5}$	$8.7^{+0.3}_{-0.4}$
$CH_3\ ^{18}OH;v=0$;	...	...	...	...
$C_2H_5OH;v=0$;	...	...	...	...
$CH_3CHO;v=0$;	328^{+8}_{-8}	$15.72^{+0.16}_{-0.28}$	$5.6^{+0.8}_{-0.7}$	$9.0^{+0.4}_{-0.3}$
$CH_3CHO;v15=1$;	435^{+9}_{-8}	$16.26^{+0.15}_{-0.22}$	$11.2^{+0.8}_{-0.8}$	$8.5^{+0.3}_{-0.4}$
$HCOOCH_3;v=0$;	396^{+10}_{-8}	$16.47^{+0.14}_{-0.26}$	$9.3^{+0.8}_{-0.6}$	$9.2^{+0.4}_{-0.3}$
$HCOOCH_3;v18=1$;	344^{+7}_{-11}	$16.69^{+0.19}_{-0.19}$	$11.5^{+0.8}_{-0.6}$	$8.9^{+0.4}_{-0.3}$
$CH_3OCH_3;v=0$;	...	...	...	...
$CH_2(OH)CHO;v=0$;	...	...	...	...
aGg'-$(CH_2OH)_2;v=0$;	...	...	...	...
$H_2CO;v=0$;	281^{+9}_{-9}	$15.98^{+0.11}_{-0.16}$	$3.6^{+0.7}_{-0.7}$	$8.5^{+0.3}_{-0.3}$
$D_2CO;v=0$;	430^{+10}_{-8}	$15.46^{+0.19}_{-0.23}$	$3.1^{+0.8}_{-0.7}$	$9.1^{+0.3}_{-0.3}$
t-HCOOH;v = 0;	...	...	...	...
$NH_2CHO;v=0$;	...	...	...	...
$HNCO;v=0$;	321^{+11}_{-8}	$15.41^{+0.19}_{-0.23}$	$10.9^{+0.7}_{-0.7}$	$9.5^{+0.4}_{-0.3}$

Table B5
(Continued)

Species	T_{ex} (K)	N ($\log_{10}(cm^{-2})$)	δv (km s^{-1})	v_{LSR} (km s^{-1})
$C_2H_5CN;v=0$;	...	...	...	...
$^{13}CH_3CN;v=0$;	...	...	...	...
$DCN;v=0$;	(100)	$14.10^{+0.18}_{-0.18}$	$6.8^{+0.8}_{-0.8}$	$9.6^{+0.5}_{-0.3}$
$HCCCN;v=0$;	(100)	$13.88^{+0.25}_{-0.21}$	$3.7^{+0.7}_{-0.7}$	$9.1^{+0.4}_{-0.3}$
$^{13}CS;v=0$;	(100)	$14.09^{+0.22}_{-0.22}$	$6.1^{+0.8}_{-0.7}$	$10.4^{+0.4}_{-0.4}$
$H_2S;v=0$;	(100)	$15.78^{+0.15}_{-0.15}$	$2.1^{+0.7}_{-0.6}$	$9.0^{+0.3}_{-0.3}$
$OCS;v=0$;	180^{+9}_{-9}	$15.52^{+0.15}_{-0.18}$	$2.4^{+0.7}_{-0.7}$	$8.9^{+0.3}_{-0.3}$
$O^{13}CS;v=0$;	...	...	...	...
$^{34}SO;v=0$;	...	...	...	...
$SO_2;v=0$;	(100)	$15.83^{+0.29}_{-0.19}$	$10.3^{+0.7}_{-0.7}$	$10.4^{+0.4}_{-0.4}$
CCD;v = 0;	...	...	...	...
c-$C_3H_2;v=0$;	...	...	...	...
$DCO^+;v=0$;	(100)	$13.37^{+0.23}_{-0.21}$	$1.1^{+0.4}_{-0.3}$	$9.1^{+0.3}_{-0.3}$
$N2D^+;v=0$;	...	...	...	...
$C^{18}O;v=0$;	(100)	$17.11^{+0.11}_{-0.16}$	$1.5^{+0.6}_{-0.3}$	$8.8^{+0.2}_{-0.3}$
SiO;v = 0;_1	(100)	$15.34^{+0.05}_{-0.05}$	$50.9^{+0.7}_{-0.9}$	$56.4^{+0.3}_{-0.4}$
SiO;v = 0;_2	(100)	$15.38^{+0.05}_{-0.05}$	$47.1^{+0.7}_{-0.6}$	$-36.4^{+72.5}_{-73.2}$

Table B6
Molecular Parameters of G208N1

Species	T_{ex} (K)	N ($\log_{10}(cm^{-2})$)	δv (km s^{-1})	v_{LSR} (km s^{-1})
$CH_3OH;v=0$;	277^{+7}_{-5}	$16.83^{+0.11}_{-0.11}$	$3.7^{+0.5}_{-0.4}$	$11.3^{+0.2}_{-0.2}$
$^{13}CH_3OH;v=0$;	223^{+6}_{-6}	$16.14^{+0.17}_{-0.14}$	$2.3^{+0.5}_{-0.5}$	$11.3^{+0.3}_{-0.3}$
$CH_2DOH;v=0$;	44^{+8}_{-5}	$16.40^{+0.17}_{-0.14}$	$1.8^{+0.5}_{-0.4}$	$11.4^{+0.3}_{-0.2}$
$CH_3\ ^{18}OH;v=0$;	116^{+7}_{-5}	$15.75^{+0.19}_{-0.16}$	$1.6^{+0.4}_{-0.4}$	$11.3^{+0.2}_{-0.3}$
$C_2H_5OH;v=0$;	342^{+6}_{-6}	$16.31^{+0.16}_{-0.11}$	$3.6^{+0.5}_{-0.5}$	$11.3^{+0.3}_{-0.2}$
$CH_3CHO;v=0$;	107^{+7}_{-6}	$15.06^{+0.14}_{-0.11}$	$2.0^{+0.5}_{-0.4}$	$11.2^{+0.3}_{-0.2}$
$CH_3CHO;v15=1$;	199^{+6}_{-6}	$15.27^{+0.17}_{-0.17}$	$3.3^{+0.5}_{-0.6}$	$11.1^{+0.3}_{-0.2}$
$HCOOCH_3;v=0$;	187^{+8}_{-6}	$16.00^{+0.10}_{-0.12}$	$1.9^{+0.4}_{-0.5}$	$11.4^{+0.2}_{-0.2}$
$HCOOCH_3;v18=1$;	262^{+7}_{-6}	$16.46^{+0.12}_{-0.14}$	$6.4^{+0.5}_{-0.4}$	$11.2^{+0.3}_{-0.2}$
$CH_3OCH_3;v=0$;	142^{+6}_{-7}	$16.26^{+0.16}_{-0.13}$	$5.6^{+0.5}_{-0.4}$	$10.8^{+0.3}_{-0.2}$
$CH_2(OH)CHO;v=0$;	313^{+6}_{-6}	$15.47^{+0.15}_{-0.18}$	$7.6^{+0.5}_{-0.5}$	$11.5^{+0.3}_{-0.3}$
aGg'-$(CH_2OH)_2;v=0$;	...	...	...	...
$H_2CO;v=0$;	373^{+40}_{-49}	$16.20^{+0.10}_{-0.10}$	$4.5^{+0.7}_{-0.8}$	$11.4^{+0.3}_{-0.2}$
$D_2CO;v=0$;	179^{+8}_{-5}	$14.63^{+0.15}_{-0.15}$	$2.1^{+0.6}_{-0.5}$	$11.6^{+0.3}_{-0.2}$
t-HCOOH;v = 0;	...	...	...	...
$NH_2CHO;v=0$;	367^{+8}_{-6}	$14.72^{+0.19}_{-0.14}$	$11.3^{+0.5}_{-0.4}$	$10.2^{+0.3}_{-0.2}$
$HNCO;v=0$;	317^{+8}_{-5}	$15.41^{+0.16}_{-0.13}$	$8.7^{+0.6}_{-0.5}$	$11.2^{+0.3}_{-0.2}$
$C_2H_5CN;v=0$;	98^{+7}_{-6}	$14.71^{+0.18}_{-0.14}$	$8.9^{+0.6}_{-0.5}$	$11.2^{+0.3}_{-0.2}$
$^{13}CH_3CN;v=0$;	395^{+8}_{-5}	$13.97^{+0.18}_{-0.15}$	$1.6^{+0.4}_{-0.4}$	$11.2^{+0.2}_{-0.3}$
$DCN;v=0$;	(100)	$13.77^{+0.16}_{-0.16}$	$6.2^{+0.5}_{-0.5}$	$11.1^{+0.3}_{-0.2}$
$HCCCN;v=0$;	(100)	$13.82^{+0.19}_{-0.16}$	$6.5^{+0.5}_{-0.5}$	$11.1^{+0.3}_{-0.2}$
$^{13}CS;v=0$;	(100)	$13.85^{+0.13}_{-0.16}$	$1.3^{+0.4}_{-0.3}$	$11.3^{+0.3}_{-0.2}$
$H_2S;v=0$;	(100)	$15.84^{+0.10}_{-0.08}$	$2.0^{+0.5}_{-0.3}$	$11.4^{+0.2}_{-0.2}$
$OCS;v=0$;	98^{+8}_{-7}	$15.37^{+0.14}_{-0.09}$	$1.9^{+0.5}_{-0.3}$	$11.4^{+0.2}_{-0.2}$
$O^{13}CS;v=0$;	20^{+5}_{-5}	$14.52^{+0.17}_{-0.17}$	$2.1^{+0.7}_{-0.4}$	$12.0^{+0.2}_{-0.3}$
$^{34}SO;v=0$;	(100)	$14.58^{+0.17}_{-0.17}$	$10.9^{+0.6}_{-0.3}$	$11.4^{+0.2}_{-0.3}$
$SO_2;v=0$;	...	...	...	...
CCD;v = 0;	...	...	...	...
c- $C_3H_2;v=0$;	...	...	...	...
$DCO^+;v=0$;	...	...	...	...
$N2D^+;v=0$;	...	...	...	...
$C^{18}O;v=0$;	(100)	$16.78^{+0.12}_{-0.10}$	$1.8^{+0.5}_{-0.4}$	$11.3^{+0.2}_{-0.2}$
$SiO;v=0$;	...	...	...	...

Table B7
Molecular Parameters of G208E

Species	T_{ex} (K)	N ($\log_{10}(cm^{-2})$)	δv (km s^{-1})	v_{LSR} (km s^{-1})
$CH_3OH;v = 0;$	154^{+20}_{-16}	$16.51^{+0.21}_{-0.40}$	$7.5^{+1.3}_{-1.6}$	$8.5^{+0.8}_{-0.6}$
$^{13}CH_3OH;v = 0;$	83^{+16}_{-20}	$15.91^{+0.26}_{-0.49}$	$11.6^{+1.5}_{-1.5}$	$6.7^{+0.9}_{-0.6}$
$CH_2DOH;v = 0;$	⋯	⋯	⋯	⋯
$CH_3\ ^{18}OH;v = 0;$	⋯	⋯	⋯	⋯
$C_2H_5OH;v = 0;$	⋯	⋯	⋯	⋯
$CH_3CHO;v = 0;$	⋯	⋯	⋯	⋯
$CH_3CHO;v15 = 1;$	⋯	⋯	⋯	⋯
$HCOOCH_3;v = 0;$	328^{+10}_{-24}	$16.48^{+0.14}_{-0.33}$	$10.3^{+1.9}_{-1.2}$	$9.8^{+0.8}_{-0.5}$
$HCOOCH_3;v18 = 1;$	⋯	⋯	⋯	⋯
$CH_3OCH_3;v = 0;$	⋯	⋯	⋯	⋯
$CH_2(OH)CHO;v = 0;$	⋯	⋯	⋯	⋯
$aGg'\text{-}(CH_2OH)_2;v = 0;$	⋯	⋯	⋯	⋯
$H_2CO;v = 0;$	323^{+18}_{-22}	$16.05^{+0.10}_{-0.23}$	$3.1^{+1.4}_{-1.0}$	$9.0^{+0.6}_{-0.5}$
$D_2CO;v = 0;$	⋯	⋯	⋯	⋯
$t\text{-}HCOOH;v = 0;$	⋯	⋯	⋯	⋯
$NH_2CHO;v = 0;$	⋯	⋯	⋯	⋯
$HNCO;v = 0;$	⋯	⋯	⋯	⋯
$C_2H_5CN;v = 0;$	⋯	⋯	⋯	⋯
$^{13}CH_3CN;v = 0;$	⋯	⋯	⋯	⋯
$DCN;v = 0;$	(100)	$13.84^{+0.24}_{-0.44}$	$3.2^{+1.7}_{-1.2}$	$9.1^{+0.6}_{-0.9}$
$HCCCN;v = 0;$	⋯	⋯	⋯	⋯
$^{13}CS;v = 0;$	⋯	⋯	⋯	⋯
$H_2S;v = 0;$	⋯	⋯	⋯	⋯
$OCS;v = 0;$	20^{+8}_{-14}	$16.36^{+0.42}_{-0.64}$	$9.3^{+1.0}_{-1.8}$	$6.6^{+0.6}_{-0.9}$
$O^{13}CS;v = 0;$	⋯	⋯	⋯	⋯
$^{34}SO;v = 0;$	(100)	$14.87^{+0.40}_{-0.33}$	$11.4^{+1.5}_{-1.5}$	$9.6^{+0.6}_{-0.8}$
$SO_2;v = 0;$	⋯	⋯	⋯	⋯
$CCD;v = 0;$	238^{+21}_{-14}	$15.18^{+0.36}_{-0.40}$	$1.9^{+1.4}_{-1.1}$	$8.8^{+0.7}_{-0.8}$
$c\text{-}C_3H_2;v = 0;$	⋯	⋯	⋯	⋯
$DCO^+;v = 0;$	⋯	⋯	⋯	⋯
$N2D^+;v = 0;$	⋯	⋯	⋯	⋯
$C^{18}O;v = 0;$	(100)	$16.73^{+0.29}_{-0.29}$	$3.0^{+1.4}_{-1.2}$	$8.8^{+0.6}_{-0.7}$
$SiO;v = 0;$	(100)	$13.89^{+0.19}_{-0.45}$	$5.0^{+1.3}_{-1.4}$	$8.6^{+0.9}_{-0.6}$

Table B8
Molecular Parameters of G209N1B

Species	T_{ex} (K)	N ($\log_{10}(cm^{-2})$)	δv (km s^{-1})	v_{LSR} (km s^{-1})
$CH_3OH;v = 0;$	119^{+19}_{-16}	$16.05^{+0.26}_{-0.38}$	$3.2^{+1.5}_{-1.3}$	$6.9^{+0.8}_{-0.6}$
$^{13}CH_3OH;v = 0;$	⋯	⋯	⋯	⋯
$CH_2DOH;v = 0;$	⋯	⋯	⋯	⋯
$CH_3\ ^{18}OH;v = 0;$	⋯	⋯	⋯	⋯
$C_2H_5OH;v = 0;$	⋯	⋯	⋯	⋯
$CH_3CHO;v = 0;$	⋯	⋯	⋯	⋯
$CH_3CHO;v15 = 1;$	⋯	⋯	⋯	⋯
$HCOOCH_3;v = 0;$	⋯	⋯	⋯	⋯
$HCOOCH_3;v18 = 1;$	⋯	⋯	⋯	⋯
$CH_3OCH_3;v = 0;$	⋯	⋯	⋯	⋯
$CH_2(OH)CHO;v = 0;$	⋯	⋯	⋯	⋯
$aGg'\text{-}(CH_2OH)_2;v = 0;$	⋯	⋯	⋯	⋯
$H_2CO;v = 0;$	133^{+14}_{-22}	$15.48^{+0.15}_{-0.12}$	$2.7^{+1.1}_{-0.6}$	$7.1^{+0.4}_{-0.3}$
$D_2CO;v = 0;$	⋯	⋯	⋯	⋯
$t\text{-}HCOOH;v = 0;$	⋯	⋯	⋯	⋯
$NH_2CHO;v = 0;$	⋯	⋯	⋯	⋯
$HNCO;v = 0;$	⋯	⋯	⋯	⋯
$C_2H_5CN;v = 0;$	⋯	⋯	⋯	⋯
$^{13}CH_3CN;v = 0;$	⋯	⋯	⋯	⋯
$DCN;v = 0;$	(100)	$13.72^{+0.18}_{-0.35}$	$2.7^{+1.7}_{-0.9}$	$7.1^{+0.7}_{-0.6}$
$HCCCN;v = 0;$	(100)	$13.42^{+0.49}_{-0.42}$	$2.4^{+1.7}_{-0.9}$	$7.6^{+0.8}_{-0.7}$
$^{13}CS;v = 0;$	⋯	⋯	⋯	⋯
$H_2S;v = 0;$	(100)	$14.63^{+0.50}_{-0.41}$	$1.9^{+1.2}_{-1.6}$	$6.6^{+0.7}_{-0.6}$
$OCS;v = 0;$	160^{+26}_{-11}	$14.84^{+0.47}_{-0.38}$	$3.7^{+1.2}_{-1.8}$	$7.2^{+0.7}_{-0.8}$
$O^{13}CS;v = 0;$	⋯	⋯	⋯	⋯
$^{34}SO;v = 0;$	⋯	⋯	⋯	⋯
$SO_2;v = 0;$	⋯	⋯	⋯	⋯
$CCD;v = 0;$	⋯	⋯	⋯	⋯
$c\text{-}C_3H_2;v = 0;$	⋯	⋯	⋯	⋯
$DCO^+;v = 0;$	(100)	$13.39^{+0.23}_{-0.35}$	$2.5^{+1.2}_{-1.5}$	$6.8^{+0.8}_{-0.5}$
$N2D^+;v = 0;$	⋯	⋯	⋯	⋯
$C^{18}O;v = 0;$	(100)	$16.78^{+0.18}_{-0.18}$	$1.4^{+0.9}_{-0.9}$	$6.9^{+0.3}_{-0.3}$
$SiO;v = 0;$	⋯	⋯	⋯	⋯

Table B9
Molecular Parameters of G209S1

Species	T_{ex} (K)	N ($\log_{10}(cm^{-2})$)	δv (km s^{-1})	v_{LSR} (km s^{-1})
$CH_3OH;v = 0;$	384^{+18}_{-18}	$16.63^{+0.25}_{-0.37}$	$5.2^{+1.1}_{-1.4}$	$6.3^{+0.4}_{-0.8}$
$^{13}CH_3OH;v = 0;$	⋯	⋯	⋯	⋯
$CH_2DOH;v = 0;$	⋯	⋯	⋯	⋯
$CH_3\ ^{18}OH;v = 0;$	⋯	⋯	⋯	⋯
$C_2H_5OH;v = 0;$	⋯	⋯	⋯	⋯
$CH_3CHO;v = 0;$	376^{+21}_{-14}	$15.58^{+0.20}_{-0.46}$	$5.7^{+1.6}_{-1.0}$	$7.4^{+0.9}_{-0.5}$
$CH_3CHO;v15 = 1;$	⋯	⋯	⋯	⋯
$HCOOCH_3;v = 0;$	⋯	⋯	⋯	⋯
$HCOOCH_3;v18 = 1;$	⋯	⋯	⋯	⋯
$CH_3OCH_3;v = 0;$	⋯	⋯	⋯	⋯
$CH_2(OH)CHO;v = 0;$	⋯	⋯	⋯	⋯
$aGg'\text{-}(CH_2OH)_2;v = 0;$	⋯	⋯	⋯	⋯
$H_2CO;v = 0;$	98^{+15}_{-19}	$15.08^{+0.19}_{-0.19}$	$3.7^{+1.8}_{-0.8}$	$6.8^{+0.7}_{-0.4}$
$D_2CO;v = 0;$	101^{+14}_{-21}	$14.29^{+0.25}_{-0.45}$	$4.3^{+2.4}_{-1.0}$	$7.3^{+0.7}_{-0.7}$
$t\text{-}HCOOH;v = 0;$	⋯	⋯	⋯	⋯
$NH_2CHO;v = 0;$	387^{+20}_{-13}	$15.01^{+0.18}_{-0.34}$	$7.3^{+1.5}_{-1.2}$	$7.3^{+0.7}_{-0.6}$
$HNCO;v = 0;$	392^{+19}_{-16}	$15.09^{+0.21}_{-0.40}$	$5.8^{+1.4}_{-1.3}$	$6.3^{+0.7}_{-0.6}$
$C_2H_5CN;v = 0;$	⋯	⋯	⋯	⋯
$^{13}CH_3CN;v = 0;$	⋯	⋯	⋯	⋯
$DCN;v = 0;$	(100)	$13.45^{+0.32}_{-0.32}$	$2.9^{+1.5}_{-1.2}$	$6.8^{+0.6}_{-0.7}$
$HCCCN;v = 0;$	⋯	⋯	⋯	⋯
$^{13}CS;v = 0;$	⋯	⋯	⋯	⋯
$H_2S;v = 0;$	(100)	$14.99^{+0.32}_{-0.39}$	$2.9^{+1.0}_{-1.5}$	$6.8^{+0.9}_{-0.5}$
$OCS;v = 0;$	47^{+16}_{-16}	$15.03^{+0.33}_{-0.46}$	$3.6^{+1.5}_{-1.2}$	$7.1^{+0.7}_{-0.6}$
$O^{13}CS;v = 0;$	⋯	⋯	⋯	⋯
$^{34}SO;v = 0;$	⋯	⋯	⋯	⋯
$SO_2;v = 0;$	⋯	⋯	⋯	⋯
$CCD;v = 0;$	⋯	⋯	⋯	⋯
$c\text{-}C_3H_2;v = 0;$	⋯	⋯	⋯	⋯
$DCO^+;v = 0;$	(100)	$13.18^{+0.22}_{-0.41}$	$1.5^{+1.0}_{-1.0}$	$7.3^{+0.4}_{-0.7}$
$N2D^+;v = 0;$	⋯	⋯	⋯	⋯
$C^{18}O;v = 0;$	(100)	$16.64^{+0.11}_{-0.26}$	$1.7^{+0.7}_{-1.1}$	$7.1^{+0.3}_{-0.4}$
$SiO;v = 0;$	⋯	⋯	⋯	⋯

Table B10
The Molecular Parameters of G210WA

Species	T_{ex} (K)	N ($\log_{10}(cm^{-2})$)	δv (km s^{-1})	v_{LSR} (km s^{-1})
CH_3OH;v = 0;	206^{+7}_{-5}	$17.44^{+0.06}_{-0.05}$	$8.8^{+0.6}_{-0.4}$	$9.0^{+0.3}_{-0.2}$
$^{13}CH_3OH$;v = 0;	305^{+7}_{-4}	$16.79^{+0.13}_{-0.16}$	$12.9^{+0.6}_{-0.4}$	$6.5^{+0.3}_{-0.2}$
CH_2DOH;v = 0;	77^{+7}_{-6}	$17.07^{+0.15}_{-0.10}$	$13.1^{+0.5}_{-0.5}$	$7.2^{+0.3}_{-0.2}$
$CH_3\ ^{18}OH$;v = 0;	…	…	…	…
C_2H_5OH;v = 0;	…	…	…	…
CH_3CHO;v = 0;	150^{+7}_{-5}	$15.71^{+0.10}_{-0.12}$	$9.8^{+0.6}_{-0.5}$	$9.5^{+0.3}_{-0.2}$
CH_3CHO;v15 = 1;	…	…	…	…
$HCOOCH_3$;v = 0;	400^{+7}_{-6}	$16.46^{+0.16}_{-0.13}$	$11.6^{+0.4}_{-0.5}$	$9.1^{+0.3}_{-0.2}$
$HCOOCH_3$;v18 = 1;	…	…	…	…
CH_3OCH_3;v = 0;	…	…	…	…
$CH_2(OH)CHO$;v = 0;	…	…	…	…
aGg'-$(CH_2OH)_2$;v = 0;	…	…	…	…
H_2CO;v = 0;	339^{+5}_{-7}	$16.74^{+0.05}_{-0.03}$	$6.6^{+0.4}_{-0.4}$	$9.2^{+0.2}_{-0.2}$
D_2CO;v = 0;	43^{+7}_{-5}	$14.50^{+0.15}_{-0.12}$	$5.0^{+0.5}_{-0.5}$	$8.9^{+0.2}_{-0.2}$
t-HCOOH;v = 0;	…	…	…	…
NH_2CHO;v = 0;	131^{+6}_{-8}	$15.11^{+0.10}_{-0.12}$	$10.9^{+0.5}_{-0.5}$	$7.3^{+0.3}_{-0.2}$
HNCO;v = 0;	204^{+6}_{-6}	$15.90^{+0.07}_{-0.10}$	$11.3^{+0.5}_{-0.5}$	$8.2^{+0.2}_{-0.3}$
C_2H_5CN;v = 0;	…	…	…	…
$^{13}CH_3CN$;v = 0;	…	…	…	…
DCN;v = 0;	(100)	$14.57^{+0.07}_{-0.10}$	$6.9^{+0.6}_{-0.5}$	$9.0^{+0.3}_{-0.2}$
HCCCN;v = 0;	(100)	$14.43^{+0.17}_{-0.09}$	$7.1^{+0.6}_{-0.4}$	$8.1^{+0.2}_{-0.2}$
^{13}CS;v = 0;	(100)	$14.35^{+0.14}_{-0.14}$	$10.2^{+0.5}_{-0.4}$	$8.3^{+0.3}_{-0.3}$
H_2S;v = 0;	(100)	$16.00^{+0.11}_{-0.11}$	$7.1^{+0.5}_{-0.4}$	$9.3^{+0.2}_{-0.2}$
OCS;v = 0;	96^{+5}_{-7}	$15.99^{+0.09}_{-0.06}$	$8.2^{+0.5}_{-0.4}$	$9.0^{+0.3}_{-0.2}$
$O^{13}CS$;v = 0;	…	…	…	…
^{34}SO;v = 0;	(100)	$15.10^{+0.15}_{-0.12}$	$10.7^{+0.4}_{-0.5}$	$7.9^{+0.3}_{-0.2}$
SO_2;v = 0;	(100)	$16.46^{+0.11}_{-0.14}$	$9.5^{+0.5}_{-0.5}$	$8.0^{+0.2}_{-0.2}$
CCD;v = 0;	…	…	…	…
c-C_3H_2;v = 0;	…	…	…	…
DCO^+;v = 0;	(100)	$13.64^{+0.17}_{-0.14}$	$4.0^{+0.5}_{-0.4}$	$8.5^{+0.3}_{-0.2}$
$N2D^+$;v = 0;	…	…	…	…
$C^{18}O$;v = 0;	(100)	$16.98^{+0.11}_{-0.13}$	$4.0^{+0.5}_{-0.4}$	$8.5^{+0.2}_{-0.2}$
SiO;v = 0;	(100)	$13.99^{+0.15}_{-0.12}$	$5.9^{+0.5}_{-0.5}$	$8.6^{+0.2}_{-0.2}$

Table B11
Molecular Parameters of G211S

Species	T_{ex} (K)	N ($\log_{10}(cm^{-2})$)	δv (km s^{-1})	v_{LSR} (km s^{-1})
CH_3OH;v = 0;	204^{+4}_{-3}	$17.46^{+0.03}_{-0.04}$	$5.7^{+0.3}_{-0.2}$	$2.8^{+0.1}_{-0.1}$
$^{13}CH_3OH$;v = 0;	223^{+3}_{-3}	$16.80^{+0.09}_{-0.07}$	$7.3^{+0.3}_{-0.2}$	$3.2^{+0.1}_{-0.1}$
CH_2DOH;v = 0;	70^{+4}_{-3}	$17.22^{+0.06}_{-0.06}$	$7.7^{+0.3}_{-0.2}$	$2.3^{+0.1}_{-0.1}$
$CH_3\ ^{18}OH$;v = 0;	…	…	…	…
C_2H_5OH;v = 0;	352^{+3}_{-4}	$16.96^{+0.07}_{-0.05}$	$10.5^{+0.2}_{-0.3}$	$3.6^{+0.1}_{-0.1}$
CH_3CHO;v = 0;	306^{+3}_{-3}	$16.36^{+0.04}_{-0.05}$	$5.4^{+0.2}_{-0.2}$	$2.2^{+0.1}_{-0.1}$
CH_3CHO;v15 = 1;	…	…	…	…
$HCOOCH_3$;v = 0;	347^{+3}_{-3}	$16.90^{+0.05}_{-0.05}$	$7.6^{+0.3}_{-0.3}$	$2.7^{+0.1}_{-0.1}$
$HCOOCH_3$;v18 = 1;	431^{+3}_{-3}	$16.97^{+0.07}_{-0.07}$	$10.4^{+0.3}_{-0.3}$	$2.7^{+0.2}_{-0.1}$
CH_3OCH_3;v = 0;	313^{+3}_{-3}	$16.63^{+0.10}_{-0.07}$	$10.5^{+0.2}_{-0.2}$	$2.6^{+0.1}_{-0.1}$
$CH_2(OH)CHO$;v = 0;	…	…	…	…
aGg'-$(CH_2OH)_2$;v = 0;	426^{+4}_{-3}	$16.59^{+0.06}_{-0.05}$	$10.3^{+0.3}_{-0.3}$	$0.6^{+0.2}_{-0.1}$
H_2CO;v = 0;	415^{+3}_{-3}	$16.81^{+0.03}_{-0.03}$	$5.3^{+0.3}_{-0.2}$	$2.9^{+0.2}_{-0.1}$
D_2CO;v = 0;	312^{+4}_{-3}	$15.59^{+0.07}_{-0.08}$	$6.5^{+0.3}_{-0.3}$	$3.5^{+0.1}_{-0.1}$
t-HCOOH;v = 0;	(100)	$15.55^{+0.08}_{-0.08}$	$8.3^{+0.2}_{-0.3}$	$2.5^{+0.1}_{-0.1}$
NH_2CHO;v = 0;	291^{+3}_{-3}	$15.53^{+0.07}_{-0.05}$	$8.1^{+0.2}_{-0.2}$	$2.1^{+0.2}_{-0.1}$
HNCO;v = 0;	307^{+4}_{-3}	$15.91^{+0.06}_{-0.06}$	$7.2^{+0.3}_{-0.3}$	$2.7^{+0.1}_{-0.2}$
C_2H_5CN;v = 0;	…	…	…	…
$^{13}CH_3CN$;v = 0;	429^{+4}_{-3}	$14.78^{+0.09}_{-0.09}$	$10.4^{+0.3}_{-0.2}$	$2.4^{+0.1}_{-0.1}$
DCN;v = 0;	(100)	$14.43^{+0.06}_{-0.07}$	$6.3^{+0.2}_{-0.3}$	$3.1^{+0.1}_{-0.1}$
HCCCN;v = 0;	(100)	$14.37^{+0.08}_{-0.08}$	$7.9^{+0.3}_{-0.2}$	$3.1^{+0.1}_{-0.1}$
^{13}CS;v = 0;	(100)	$14.22^{+0.10}_{-0.07}$	$6.5^{+0.3}_{-0.2}$	$2.0^{+0.1}_{-0.1}$
H_2S;v = 0;	(100)	$16.00^{+0.06}_{-0.07}$	$5.5^{+0.3}_{-0.2}$	$2.7^{+0.1}_{-0.1}$
OCS;v = 0;	254^{+4}_{-3}	$16.16^{+0.05}_{-0.05}$	$6.0^{+0.3}_{-0.2}$	$2.7^{+0.1}_{-0.1}$
$O^{13}CS$;v = 0;	310^{+3}_{-3}	$15.28^{+0.08}_{-0.08}$	$7.4^{+0.3}_{-0.2}$	$4.3^{+0.1}_{-0.1}$
^{34}SO;v = 0;	(100)	$14.94^{+0.08}_{-0.08}$	$8.0^{+0.3}_{-0.2}$	$2.3^{+0.2}_{-0.1}$
SO_2;v = 0;	(100)	$16.03^{+0.07}_{-0.09}$	$7.3^{+0.2}_{-0.3}$	$3.4^{+0.1}_{-0.1}$
CCD;v = 0;	…	…	…	…
c-C_3H_2;v = 0;	…	…	…	…
DCO^+;v = 0;	(100)	$13.48^{+0.09}_{-0.09}$	$8.1^{+0.2}_{-0.2}$	$2.5^{+0.2}_{-0.1}$
$N2D^+$;v = 0;	…	…	…	…
$C^{18}O$;v = 0;	(100)	$16.99^{+0.08}_{-0.07}$	$4.9^{+0.3}_{-0.3}$	$3.3^{+0.1}_{-0.1}$
SiO;v = 0;	(100)	$13.83^{+0.10}_{-0.06}$	$14.5^{+0.2}_{-0.3}$	$2.0^{+0.2}_{-0.1}$

Table B12
List of All Identified Transitions

Chemical Name	Species	f_{rest} (MHz)	A_{ij} (s^{-1})	E_{up} (K)	g_{up}	Quantum Numbers	Reference
Methanol	CH_3OH	216945.6	1.2135E-05	55.9	44	rovibSym=E; v12 = 0; J = 5-4; Ka=1-2; Kc=4-3	XCDMS-1370
	CH_3OH	218440.0	4.6863E-05	45.5	36	rovibSym=E; v12 = 0; J = 4-3; Ka=2-1; Kc=3-2	XCDMS-1370
	CH_3OH	231281.1	1.8314E-05	165.3	84	rovibSym=A2; v12 = 0; J = 10-9; Ka=2-3; Kc=9-6	XCDMS-1370
	CH_3OH	232418.6	1.8675E-05	165.4	84	rovibSym=A1; v12 = 0; J = 10-9; Ka=2-3; Kc=8-7	XCDMS-1370
	CH_3OH	232783.5	2.1649E-05	446.5	148	rovibSym=A1; v12 = 0; J = 18-17; Ka=3-4; Kc=16-13	XCDMS-1370
	CH_3OH	232945.0	2.1267E-05	190.4	84	rovibSym=E; v12 = 0; J = 10-11; Ka=3-2; Kc=7-9	XCDMS-1370
	CH_3OH	233795.8	2.1978E-05	446.6	148	rovibSym=A2; v12 = 0; J = 18-17; Ka=3-4; Kc=15-14	XCDMS-1370

Note. A_{ij} is the Einstein coefficient in hertz. E_{up} is the upper level of the transition in kelvin. g_{up} is the degeneracy of the upper state. The last column is the species ID in the XCLASS. This table is published in its entirety in machine-readable form.

(This table is available in its entirety in machine-readable form.)

Appendix C
SED Analysis

All of the photometric data points we use for SED fitting can be found in Table 6 of Dutta et al. (2020). In this section, Table C1 shows the wavelength, the aperture, instrument, and the observatory for each SED photometric data points. Appendix C.1 explains how we derive and apply the additional constraint for the cavity of the YSO model. Table C2 shows the related cavity parameters (e.g., opening angle and position angle), and Figure C2 shows the CO $J = 2 - 1$ outflow as well as the cavity wall exported by the SED Fitter. Table C3 displays the parameters of the five best-fit HO-CHUNK YSO models exported by the SED Fitter. They can be used as the input parameters for the HO-CHUNK simulation. There are some limitations in reproducing the original YSO model SEDs, and Appendix C.2 explains those limitations. Figure C1 shows the SED data points from the observation and the best-fit SED curves obtained by the SED Fitter.

C.1. Additional Constraint to the Cavity of the YSO Model

We aimed to derive the effective opening angle for an additional constraint to the YSO model. The shape of the cavity wall is described as:

$$z = a\tilde{r}^b + z_0, \tag{C1}$$

where z and $\tilde{r}$ are the height and the radial distance in cylindrical coordinates, respectively, z_0 is the offset of the cavity, b is the polynomial index assumed to be 1.5, and a is a parameter correlated with the opening angle (θ). The opening angle θ of the cavity in the HO-CHUNK is defined by:

$$\tan\theta \equiv \frac{\tilde{r}_{max}}{z_{max}}, \tag{C2}$$

where $\tilde{r}_{max}$ is the outer radius of the envelope, and $z_{max} = z(\tilde{r}_{max})$. Due to the inclination, the effective height Z in the observation needs to be corrected by:

$$Z = z\cos(90^\circ - \varphi), \tag{C3}$$

where φ is the inclination angle, and the effective opening angle (Θ) is therefore:

$$\tan\Theta = \frac{\tan\theta}{\cos(90^\circ - \varphi)}. \tag{C4}$$

From Dutta et al. (2020), we adopt the effective opening angle at 400 au (Θ_{400}) where Θ_{400} is defined by:

$$\Theta_{400} \equiv \tan^{-1}\left(\frac{\tilde{r}}{Z}\right)\Bigg|_{Z=400}. \tag{C5}$$

For the two sources whose Θ_{400}were not reported by Dutta et al. (2020), namely G208N1 and G211S, we follow a similar procedure to that in Dutta et al. (2020) to derive their Θ_{400}. We ruled out the YSO models with an effective opening angle 1° apart from our observed values (i.e., kept those with $|\Theta_{400}^{Fitter} - \Theta_{400}^{obs}| < 1^\circ$). Table C2 shows the position angle and the opening angles of the cavities in the hot corino source. Figure C2 illustrates the bipolar polynomial curves in the form of Equation (C1).

C.2. Limitation for Reproducing YSO Model SEDs

The limitations basically come from two sources. First, the version of HO-CHUNK code for making the R06 grid is no longer available. The updates, based on the change log of the version 2008, include updates of: the dust grain model file for correctly extrapolating toward 3.6 mm; and the temperature calculation for the first absorption. Second, some input parameters for the HO-CHUNK are not directly provided by the R06 grid while some of them are described in Robitaille et al. (2006, 2007). In the following, we introduce how we derive the input parameters that are not directly provided by the R06 grid.

1. *Stellar Photosphere Model*: We interpolate the stellar atmospheric model by the model grid adopted from Brott & Hauschildt (2005) to the relevant stellar temperature and surface gravity for each YSO model, and the metallicity was assumed to be the solar metallicity. The Brott & Hauschildt (2005) model grid was created with PHOENIX version AMES-cond-v2.6 (Brott & Hauschildt 2005; Husser et al. 2013), which can be downloaded via FTP[28].
2. *Dust Grain Models*: There are four input dust grain models in the HO-CHUNK code, which are that at the inner (denser) region and the outer (less dense) region of the disk, the envelope, and the outflow. For the inner disk region, the model is the "Model I" in Wood et al. (2002; or the "Disk midplane" model in Table 3 of Whitney et al. 2003), which fits the SED of an edge-on classical T Tauri star, HH 30 IRS. The size distribution from 50 μm to 1 mm is in the

[28] ftp.hs.uni-hamburg.de/pub/outgoing/phoenix/GAIA_I/GAIA_Grid_v2.6.1/2A_Res

Table C1
Information of the Observation for SED

Observatory	UKIRT	WISE	Spitzer	Spitzer	AKARI PSC
Filter or Band	UKIDSS *K*	W1, W2, W3, W4	IRAC	MIPS	IRC S9W, L18W
Wavelength (μm)	2.2	3.4, 4.6, 12, 22	3.6, 4.5, 5.8	24	9, 18
Aperture	4.″0	6.″0	2.″4	6.″0	5.″5, 5.″7
Observatory	AKARI BSC	Herschel	APEX	JCMT	ALMA
Filter or Band	FIS N60, WIDE-L, N160	PACS	SABOCA, LABOCA	SCUBA2 850	Band 6
Wavelength (μm)	65, 140, 160	70, 100, 160	350, 870	850	1300
Aperture	7.″5	9.″6, 9.″6, 12.″8	7.″3, 19.″0	14.″0	∼0.″35, ∼6.″0

Note. The SED flux data points were collected from Dutta et al. (2020).
References. UKIRT/UKIDSS: Lawrence et al. (2007); WISE: Wright et al. (2010) Spitzer: Werner et al. (2004); IRAC: Fazio et al. (2004); MIPS: Rieke et al. (2004); AKARI PSC: Ishihara et al. (2010); AKARI BSC: Oyabu (2010); Herschel: Pilbratt et al. (2010); PACS: Poglitsch et al. (2010); APEX: Güsten et al. (2006); SABOCA: Siringo et al. (2010); LABOCA: Siringo et al. (2009); JCMT/SCUBA2: Di Francesco et al. (2008).

Table C2
Comparison of the Cavity Parameters Derived from Different Methods

Name	PA (deg)	$\theta^{\rm Fitter}$ (deg)	$\Theta^{\rm Fitter}$ (deg)	$\Theta_{400}^{\rm Fitter}$ (deg)	$\Theta_{400}^{\rm Dutta}$ (deg)
G192	132	23	32	60	61
G196A	…	…	…	…	54
G203W2	…	…	…	…	48
G205S1A	72	7	12	35	34
G206W2	76	3	10	39	38
G208E	…	…	…	…	41
G208N1	85	8	11	29	29[a]
G209N1B	82	18	31	64	…
G209S1	51	11	11	31	31
G210WA	78	20	26	53	53
G211S	146	11	11	35	36[a]

Note. PA is the position angle. θ is the opening angle of the cavity. Θ and Θ_{400} are the effective opening angles at $z = z_{\rm max}$ and 400 au. $\Theta^{\rm Dutta}$ is the opening angle adapted from Dutta et al. (2020). "Fitter" represents the best-fit model fit by SED Fitter.
[a] Fitted by this study.

form of:

$$n(a)da = C_i\, a^{-p} \exp\left[-\left(\frac{a}{a_{\rm min}}\right)^q\right] da, \tag{C6}$$

where n is the distribution function, a is the grain size, and C_i, p, and q are adapted from Wood et al. (2002). For the other three regions, the model is the "Outflow" model in Table 3 of Whitney et al. (2003), which has a size distribution fitting a ratio of total-to-selective extinction R_V (i.e., "KMH" model presented by Kim et al. 1994). The R_V is 3.6, which is slightly larger than that of the canonical sight line ($R_V = 3.1$). The boundary between the inner and the outer region of the disk is defined with the density of the molecular hydrogen $n({\rm H_2}) > 10^{10}\,{\rm cm^{-3}}$ (i.e., $\rho > 3.35 \times 10^{-14}\,{\rm g\,cm^{-3}}$).

3. *Magnetospheric accretion*: The magnetospheric truncation radius $R_{\rm trunc}$ and the fractional area of the hot spot ($f_{\rm spot}$) are user defined; however, we do not find the value applied by the SED Fitter from Robitaille et al. (2006). We therefore applied the default value of the HO-CHUNK 2004 release according to the change log of the HO-CHUNK 2008 version: $R_{\rm trunc} = 5R_\star$ and $f_{\rm spot} = 0.007$. Note that the latter is the mean value of Calvet & Gullbring (1998), which works on the accretion shock models for the infalling accretion flow in magnetosphere surrounding classical T Tauri stars.
4. Foreground extinction: SED Fitter introduces a foreground extinction A_V, and the flux density is affected by:

$$\log_{10} F_\lambda^{\rm obs} = \log_{10} F_\lambda - 0.4 A_V \frac{\kappa_\lambda}{\kappa_V}, \tag{C7}$$

where κ_λ and κ_V are the opacity at the examined wavelength and 0.55 μm, respectively. The extinction law model is exported from the SED Fitter code, and it was derived by fitting a galactic ISM curve modified for the mid-IR band (Indebetouw et al. 2005) with the method in Kim et al. (1994).

Table C3
Parameters of the Five Best SED Fitter Models

Source	Model	#	chi2	Av	$L_{\rm tot}$	$t_\star$ yr	$M_\star$ $M_\odot$	$R_\star$ $R_\odot$	$T_\star$ K	$M_{\rm disk}$ $M_\odot$	$\dot{M}_{\rm disk}$ $M_\odot {\rm yr}^{-1}$	$R^{\rm inner}$ $R_{\rm sub}$	$R^{\rm outer}_{\rm disk}$ au	$\dot{M}_{\rm env}$ $M_\odot {\rm yr}^{-1}$	$R^{\rm outer}_{\rm env}$ au	θ {°}	cos φ	$\rho_{\rm cav}$ g cm^{-3}	$\rho_{\rm amb}$ g cm^{-3}
G192	30110098	9	356.445	19.942	8.65	26800	0.736	6.324	3928	1.03E-02	3.13E-08	1.0	73.32	1.47E-04	5529	22.55	0.75	8.84E-21	4.54E-22
	30004555	9	476.747	25.581	17.46	114800	1.280	7.658	4214	5.07E-03	1.90E-07	1.0	76.81	1.25E-04	3399	35.42	0.45	2.98E-21	8.21E-22
	30111619	9	504.379	30.059	6.96	23180	0.542	5.538	3776	3.79E-03	5.07E-07	1.0	14.12	1.43E-04	5518	19.79	0.85	3.35E-20	1.65E-22
	30004556	9	1017.876	38.539	17.46	114800	1.280	7.658	4214	5.07E-03	1.90E-07	1.0	76.81	1.25E-04	3399	35.42	0.55	2.98E-21	8.21E-22
	30148869	9	1314.257	16.334	5.76	9730	0.485	5.813	3689	3.04E-02	6.92E-08	8.99	53.09	1.29E-04	8806	15.83	0.85	1.26E-20	1.04E-22
G205S1A	30168999	15	3283.434	1.279	37.74	3505	1.351	12.340	4064	9.78E-03	1.53E-07	1.0	18.07	1.59E-04	2874	6.50	0.85	2.66E-20	4.70E-22
	300005210	15	4379.332	35.234	22.23	11260	1.017	9.814	3999	6.65E-03	4.42E-08	1.0	18.04	1.18E-04	3123	3.53	0.95	4.74E-20	4.33E-22
	301481210	15	4981.519	25.538	9.32	9795	0.629	7.018	3809	3.83E-04	6.69E-09	1.0	21.78	5.87E-05	2501	4.00	0.95	2.72E-20	4.02E-22
	30052308	15	5310.032	0.855	26.98	4341	1.038	10.880	3977	3.73E-02	1.43E-07	1.0	18.71	1.02E-04	1754	10.11	0.75	1.95E-20	2.23E-22
	30029961	15	5409.914	2.349	25.83	14180	1.414	9.678	4181	2.00E-02	3.23E-08	1.642	52.16	6.01E-05	2982	11.56	0.05	5.67E-20	4.01E-22
G206W2	300261810	10	3104.624	164.322	23.03	2008	0.927	10.320	3923	2.94E-02	1.71E-07	6.048	13.67	4.48E-04	6461	3.17	0.95	2.27E-20	3.54E-22
	300775310	10	4999.664	160.318	26.76	1838	1.073	10.680	4008	3.52E-03	1.28E-07	3.703	5.87	1.55E-04	8718	2.51	0.95	3.03E-20	4.57E-22
	30068109	10	5447.386	202.478	34.30	2089	0.737	8.435	3848	9.22E-02	8.45E-06	1.0	4.98	1.75E-05	2031	8.77	0.85	1.97E-20	3.70E-22
	30091768	10	5670.928	233.681	83.12	2644	1.291	14.530	3969	2.73E-02	1.49E-05	1.0	3.93	1.02E-05	13520	4.37	0.75	1.75E-20	2.77E-22
	30075069	10	5863.251	232.446	80.85	12800	2.036	14.280	4215	1.18E-01	5.97E-06	1.0	10.15	2.53E-05	3522	6.69	0.85	8.94E-21	6.09E-22
G208N1	30171007	15	4551.015	22.018	130.70	1486	1.000	12.900	3884	2.68E-02	4.55E-05	1.0	1.59	1.59E-04	1674	8.46	0.65	7.44E-20	6.61E-22
	30193948	15	8440.588	40.363	112.20	3691	2.283	19.420	4137	1.56E-01	4.07E-06	1.0	4.29	8.80E-05	2664	6.23	0.75	1.97E-20	1.20E-21
	30147519	15	12921.615	13.108	53.71	2673	0.895	9.212	3937	1.04E-01	1.33E-05	1.0	6.57	2.02E-04	1178	6.84	0.85	7.71E-20	4.75E-22
	30193247	15	14046.726	34.773	76.63	1403	1.674	13.720	4134	4.87E-02	8.44E-06	1.389	2.42	5.48E-05	4682	5.14	0.65	4.65E-20	4.93E-22
	30042819	15	14241.034	16.968	38.74	2137	0.420	6.304	3573	2.33E-02	1.77E-05	1.0	2.49	7.44E-05	1348	7.04	0.85	1.89E-20	2.11E-22
G209N1B	30120589	16	3257.637	12.456	6.18	118300	0.748	5.151	4004	6.61E-04	1.49E-08	1.0	42.36	1.17E-04	8746	17.76	0.85	7.44E-21	1.78E-22
	301073310	16	3372.405	22.544	2.51	29560	0.348	4.359	3476	3.12E-04	9.77E-09	1.0	29.98	1.25E-04	3644	16.78	0.95	1.89E-20	1.34E-22
	30186318	16	3380.836	14.018	6.16	16960	0.542	5.842	3764	9.36E-04	2.01E-09	1.0	86.70	6.04E-05	4201	22.54	0.75	1.42E-20	1.07E-22
	301051110	16	3477.510	24.504	2.77	47640	0.417	4.222	3620	6.63E-04	6.25E-09	1.0	78.66	1.36E-04	3817	17.71	0.95	4.71E-21	1.54E-22
	30110939	16	3502.317	15.991	4.49	9906	0.393	5.540	3546	5.39E-04	6.84E-08	1.087	10.13	6.09E-05	5026	18.41	0.85	6.06E-20	1.10E-22
G209S1	30119282	18	3415.220	5.028	18.98	5267	0.465	6.087	3651	2.28E-02	6.44E-06	1.754	8.25	2.37E-05	2419	10.67	0.15	1.48E-20	1.84E-22
	30083783	18	3420.874	6.633	13.86	33880	0.834	6.391	4012	4.66E-02	1.33E-06	8.829	17.64	2.34E-05	2411	10.17	0.25	2.49E-20	2.09E-22
	30059808	18	3682.985	6.121	17.96	27780	1.145	8.213	4125	1.30E-03	1.16E-07	1.0	16.98	7.88E-05	1413	9.39	0.75	4.23E-20	2.52E-22
	30083782	18	3769.373	5.959	13.86	33880	0.834	6.391	4012	4.66E-02	1.33E-06	8.829	17.64	2.34E-05	2411	10.17	0.15	2.49E-20	2.09E-22
	30119283	18	3905.069	5.476	18.98	5267	0.465	6.087	3651	2.28E-02	6.44E-06	1.754	8.25	2.37E-05	2419	10.67	0.25	1.48E-20	1.84E-22
G210WA	30174457	17	8439.560	6.493	42.89	26680	1.975	11.860	4276	8.33E-02	1.55E-07	4.538	104.40	1.50E-04	4044	19.93	0.65	1.44E-20	8.54E-22
	30040215	17	9277.259	7.012	55.95	10530	1.315	11.610	4072	4.64E-02	7.51E-06	1.348	10.63	6.96E-05	8874	16.90	0.45	7.29E-20	3.36E-22
	30179766	17	9523.582	20.464	23.33	262500	2.471	7.392	4591	1.07E-01	1.81E-07	2.871	127.40	5.05E-05	2872	25.48	0.55	2.95E-21	1.33E-21
	30129478	17	9821.316	0.000	38.81	6727	1.181	11.170	4032	2.66E-02	3.41E-06	4.227	6.00	1.08E-04	11500	11.00	0.75	6.50E-20	2.37E-22
	30040214	17	10155.993	4.526	55.95	10530	1.315	11.610	4072	4.64E-02	7.51E-06	1.348	10.63	6.96E-05	8874	16.90	0.35	7.29E-20	3.36E-22
G211S	30126313	17	6055.181	12.285	141.20	8642	2.829	19.120	4242	6.66E-02	9.30E-06	5.658	42.33	9.40E-05	3817	10.58	0.25	1.28E-20	1.05E-21
	30172775	17	7948.439	15.047	129.70	7524	3.368	20.640	4290	5.27E-03	4.59E-08	5.479	9.75	9.84E-05	3375	10.96	0.45	4.76E-20	1.95E-21
	30126315	17	8019.270	15.346	141.20	8642	2.829	19.120	4242	6.66E-02	9.30E-06	5.658	42.33	9.40E-05	3817	10.58	0.45	1.28E-20	1.05E-21
	30126314	17	8119.271	13.117	141.20	8642	2.829	19.120	4242	6.66E-02	9.30E-06	5.658	42.33	9.40E-05	3817	10.58	0.35	1.28E-20	1.05E-21
	30080897	17	10187.777	16.364	166.90	2401	3.483	23.660	4242	1.06E-02	1.06E-06	1.0	3.16	1.06E-04	11730	4.93	0.65	3.19E-20	7.33E-22

Note. # is the number of the SED data points. $A_{\rm V}$ is the foreground extinction. $L_{\rm tot}$ is the total luminosity. $t_\star$, $M_\star$, $R_\star$, and $T_\star$ are the age, the mass, the radius, and the temperature of central protostar, respectively. $M_{\rm disk}$ is the total mass of disk. $\dot{M}_{\rm disk}$ and $\dot{M}_{\rm env}$ are the mass accretion rate of the disk and the infall rate of the envelope, respectively. $R^{\rm inner}$ is the inner radius of both the envelope and disk. $R_{\rm sub}$ is sublimation radius. $R^{\rm outer}_{\rm disk}$ and $R^{\rm outer}_{\rm env}$ are, respectively, the outer radius of the disk and the envelope. θ and φ are the opening angle and the inclination of the cavity, respectively. $\rho_{\rm cav}$ and the $\rho_{\rm amb}$ are, respectively, cavity density and ambient density.

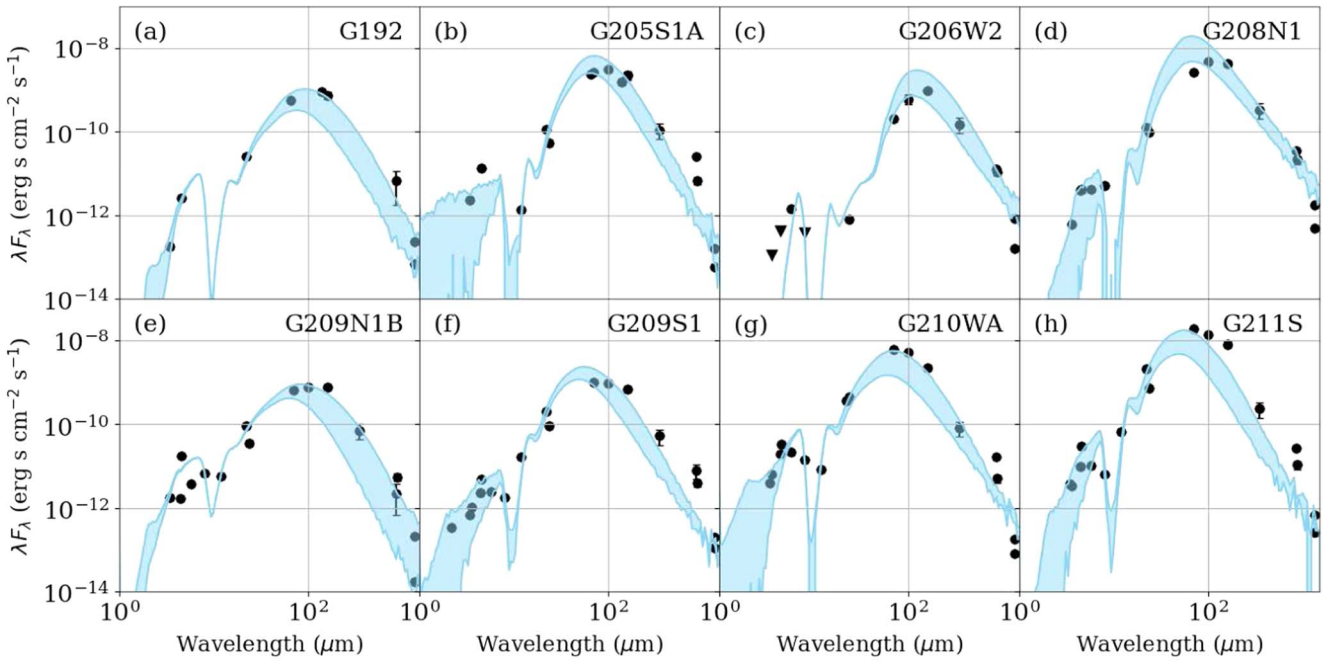

Figure C1. The observed SED data points of the hot corino sources and the best-fit curves obtained from the SED Fitter for the corresponding sources. The black dots and triangles represent the observed SED data points and the upper limits, respectively, at their corresponding wavelengths. The blue shaded regions illustrate the SED profile exported by the SED Fitter. The lower and the upper boundaries of the shaded regions represent the flux observed by the minimum and the maximum apertures, respectively (i.e., $0\farcs4$ and $19''$, respectively, multiplied by their distance $d \sim 400$ pc).

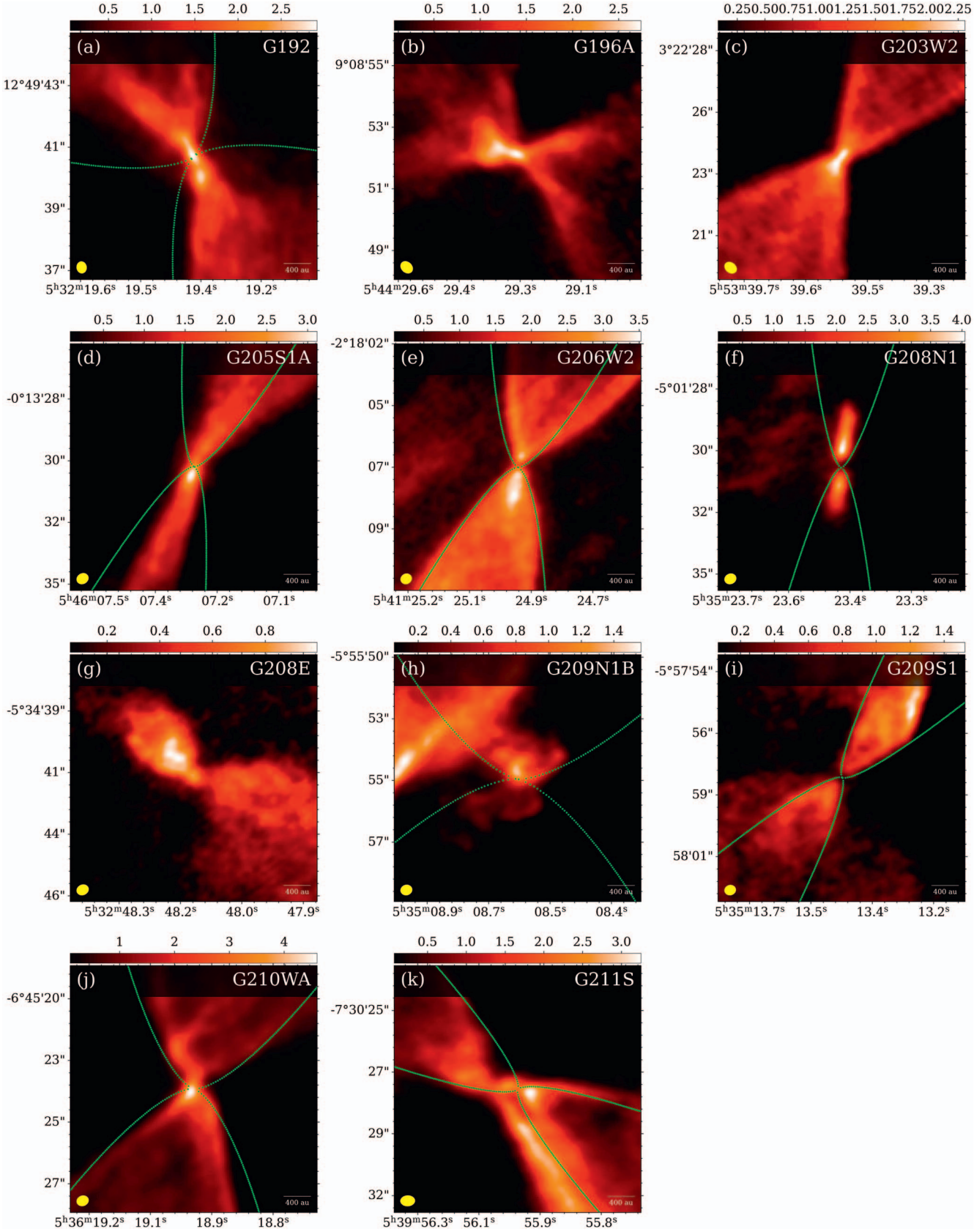

Figure C2. Moment-0 image of CO $J = 2 - 1$ transition (E_{up}=21 K and f_{rest}=231281 MHz). The green curves represent the cavity walls obtained from the SED Fitter.

ORCID iDs

Shih-Ying Hsu https://orcid.org/0000-0002-1369-1563
Sheng-Yuan Liu https://orcid.org/0000-0003-4603-7119
Tie Liu https://orcid.org/0000-0002-5286-2564
Dipen Sahu https://orcid.org/0000-0002-4393-3463
Chin-Fei Lee https://orcid.org/0000-0002-3024-5864
Kenichi Tatematsu https://orcid.org/0000-0002-8149-8546
Kee-Tae Kim https://orcid.org/0000-0003-2412-7092
Naomi Hirano https://orcid.org/0000-0001-9304-7884
Yao-Lun Yang https://orcid.org/0000-0001-8227-2816
Doug Johnstone https://orcid.org/0000-0002-6773-459X
Hongli Liu https://orcid.org/0000-0003-3343-9645
Mika Juvela https://orcid.org/0000-0002-5809-4834
Leonardo Bronfman https://orcid.org/0000-0002-9574-8454
Huei-Ru Vivien Chen https://orcid.org/0000-0002-9774-1846
Somnath Dutta https://orcid.org/0000-0002-2338-4583
David J. Eden https://orcid.org/0000-0002-5881-3229
Kai-Syun Jhan https://orcid.org/0000-0003-2069-1403
Yi-Jehng Kuan https://orcid.org/0000-0002-4336-0730
Chang Won Lee https://orcid.org/0000-0002-3179-6334
Jeong-Eun Lee https://orcid.org/0000-0003-3119-2087
Shanghuo Li https://orcid.org/0000-0003-1275-5251
Chun-Fan Liu https://orcid.org/0000-0002-1624-6545
Sheng-Li Qin https://orcid.org/0000-0003-2302-0613
Patricio Sanhueza https://orcid.org/0000-0002-7125-7685
Hsien Shang https://orcid.org/0000-0001-8385-9838
Archana Soam https://orcid.org/0000-0002-6386-2906
Alessio Traficante https://orcid.org/0000-0003-1665-6402
Jianjun Zhou https://orcid.org/0000-0003-0356-818X

References

Arce, H. G., Jørgensen, J. K., Tafalla, M., & Bachiller, R. 2008, ApJL, 681, L21
Astropy Collaboration, Robitaille, T. P., Tollerud, E. J., et al. 2013, A&A, 558, A33
Bacmann, A., Taquet, V., Faure, A., Kahane, C., & Ceccarelli, C. 2012, A&A, 541, L12
Beckwith, S. V. W., Sargent, A. I., Chini, R. S., & Guesten, R. 1990, AJ, 99, 924
Belloche, A., Müller, H. S. P., Garrod, R. T., & Menten, K. M. 2016, A&A, 587, A91
Belloche, A., Maury, A. J., Maret, S., et al. 2020, A&A, 635, A198
Bergner, J. B., Öberg, K. I., Garrod, R. T., & Graninger, D. M. 2017, ApJ, 841, 120
Bergner, J. B., Martín-Doménech, R., Öberg, K. I., et al. 2019, ESC, 3, 1564
Bianchi, E., Codella, C., Ceccarelli, C., et al. 2019, MNRAS, 483, 1850
Bianchi, E., Chandler, C. J., Ceccarelli, C., et al. 2020, MNRAS, 498, L87
Bottinelli, S., Ceccarelli, C., Neri, R., et al. 2004, ApJL, 617, L69
Brott, I., & Hauschildt, P. H. 2005, A PHOENIX Model Atmosphere Grid for Gaia, arXiv:astro-ph/0503395
Calcutt, H., Jørgensen, J. K., Müller, H. S. P., et al. 2018, A&A, 616, A90
Calvet, N., & Gullbring, E. 1998, ApJ, 509, 802
Cazaux, S., Tielens, A. G. G. M., Ceccarelli, C., et al. 2003, ApJL, 593, L51
Ceccarelli, C. 2004, in ASP Conf. Proc. 323, Star Formation in the Interstellar Medium: In Honor of David Hollenbach, Chris McKee and Frank Shu, ed. D. Johnstone et al. (San Francisco, CA: ASP), 195
Chini, R., Reipurth, B., Ward-Thompson, D., et al. 1997, ApJL, 474, L135
Codella, C., Ceccarelli, C., Cabrit, S., et al. 2016, A&A, 586, L3
Coutens, A., Commerçon, B., & Wakelam, V. 2020, A&A, 643, A108
Coutens, A., Jørgensen, J. K., van der Wiel, M. H. D., et al. 2016, A&A, 590, L6
De Simone, M., Ceccarelli, C., Codella, C., et al. 2020, ApJL, 896, L3
Di Francesco, J., Johnstone, D., Kirk, H., MacKenzie, T., & Ledwosinska, E. 2008, ApJS, 175, 277
Drozdovskaya, M. N., Walsh, C., Visser, R., Harsono, D., & van Dishoeck, E. F. 2015, MNRAS, 451, 3836
Dunham, M. M., Crapsi, A., Evans Ii, N. J., et al. 2008, ApJS, 179, 249
Dutta, S., Lee, C.-F., Liu, T., et al. 2020, ApJS, 251, 20
Eden, D. J., Liu, T., Kim, K.-T., et al. 2019, MNRAS, 485, 2895
Evans, N. J., Francesco, J. D., Lee, J.-E., et al. 2015, ApJ, 814, 22
Evans, Ii, N., Allen, L., Blake, G., et al. 2003, PASP, 115, 965
Fazio, G. G., Hora, J. L., Allen, L. E., et al. 2004, ApJS, 154, 10
Feddersen, J. R., Arce, H. G., Kong, S., et al. 2020, ApJ, 896, 11
Fischer, W. J., Megeath, S. T., Ali, B., et al. 2010, A&A, 518, L122
Fischer, W. J., Megeath, S. T., Stutz, A. M., et al. 2013, AN, 334, 53
Furlan, E., Fischer, W. J., Ali, B., et al. 2016, ApJS, 224, 5
Garrod, R. T., & Herbst, E. 2006, A&A, 457, 927
Garrod, R. T., Widicus Weaver, S. L., & Herbst, E. 2008, ApJ, 682, 283
Güsten, R., Nyman, L., Schilke, P., et al. 2006, A&A, 454, L13
Herbst, E., & van Dishoeck, E. F. 2009, ARA&A, 47, 427
Higuchi, A. E., Sakai, N., Watanabe, Y., et al. 2018, ApJS, 236, 52
Hsu, S.-Y., Liu, S.-Y., Liu, T., et al. 2020, ApJ, 898, 107
Huang, H.-C., Kuan, Y.-J., Charnley, S. B., et al. 2005, AdSpR, 36, 146
Husser, T. O., Wende-von Berg, S., Dreizler, S., et al. 2013, A&A, 553, A6
Imai, M., Sakai, N., Oya, Y., et al. 2016, ApJL, 830, L37
Indebetouw, R., Mathis, J. S., Babler, B. L., et al. 2005, ApJ, 619, 931
Ishihara, D., Onaka, T., Kataza, H., et al. 2010, A&A, 514, A1
Jacobsen, S. K., Jørgensen, J. K., Di Francesco, J., et al. 2019, A&A, 629, A29
Jørgensen, J. K., Müller, H. S. P., Calcutt, H., et al. 2018, A&A, 620, A170
Juvela, M., He, J., Pattle, K., et al. 2018, A&A, 612, A71
Kahane, C., Jaber Al-Edhari, A., Ceccarelli, C., et al. 2018, ApJ, 852, 130
Kang, M., Lee, J.-E., Choi, M., et al. 2013, ApJS, 209, 25
Kauffmann, J., Bertoldi, F., Bourke, T. L., Evans, N. J., & Lee, C. W. 2008, A&A, 487, 993
Kim, G., Tatematsu, K., Liu, T., et al. 2020, ApJS, 249, 33
Kim, S.-H., Martin, P. G., & Hendry, P. D. 1994, ApJ, 422, 164
Kong, S., Arce, H. G., Feddersen, J. R., et al. 2018, ApJS, 236, 25
Kounkel, M., Megeath, S. T., Poteet, C. A., Fischer, W. J., & Hartmann, L. 2016, ApJ, 821, 52
Kounkel, M., Covey, K., Suárez, G., et al. 2018, AJ, 156, 84
Kuan, Y.-J., Huang, H.-C., Charnley, S. B., et al. 2004, ApJL, 616, L27
Lawrence, A., Warren, S. J., Almaini, O., et al. 2007, MNRAS, 379, 1599
Lee, C.-F., Codella, C., Li, Z.-Y., & Liu, S.-Y. 2019a, ApJ, 876, 63
Lee, C.-F., Li, Z.-Y., Ho, P. T. P., et al. 2017, ApJ, 843, 27
Lee, J.-E., Lee, S., Baek, G., et al. 2019b, NatAs, 3, 314
Lee, Y.-H., Johnstone, D., Lee, J.-E., et al. 2021, ApJ, 920, 119
Liu, T., Kim, K.-T., Juvela, M., et al. 2018, ApJS, 234, 28
Lo, K. Y., Burke, B. F., & Haschick, A. D. 1975, ApJ, 202, 81
López-Sepulcre, A., Balucani, N., Ceccarelli, C., et al. 2019, ESC, 3, 2122
López-Sepulcre, A., Jaber, A. A., Mendoza, E., et al. 2015, MNRAS, 449, 2438
Mairs, S., Bell, G. S., Johnstone, D., et al. 2018, ATel, 11583, 1
Manigand, S., Jørgensen, J. K., Calcutt, H., et al. 2020, A&A, 635, A48
Martín-Doménech, R., Bergner, J. B., Öberg, K. I., et al. 2021, ApJ, 923, 155
McMullin, J. P., Waters, B., Schiebel, D., Young, W., & Golap, K. 2007, in ASP Conf. Ser. 376, Astronomical Data Analysis Software and Systems XVI, ed. R. A. Shaw, F. Hill, & D. J. Bell (San Francisco, CA: ASP), 127
Megeath, S. T., Gutermuth, R., Muzerolle, J., et al. 2012, AJ, 144, 192
Müller, H. S., Schlöder, F., Stutzki, J., & Winnewisser, G. 2005, JMoSt, 742, 215
Müller, H. S. P., Belloche, A., Xu, L.-H., et al. 2016, A&A, 587, A92
Möller, T., Endres, C., & Schilke, P. 2017, A&A, 598, A7
Nagy, Z., Menechella, A., Megeath, S. T., et al. 2020, A&A, 642, A137
Nazari, P., van Gelder, M. L., van Dishoeck, E. F., et al. 2021, A&A, 650, A150
Ortiz-León, G. N., Loinard, L., Dzib, S. A., et al. 2018, ApJ, 865, 73
Oyabu, S., Yamamura, I., Alfageme, C., et al. 2010, Proc. SPIE, 7731, 77312P
Persson, M. V., Jørgensen, J. K., Müller, H. S. P., et al. 2018, A&A, 610, A54
Pickett, H., Poynter, R., Cohen, E., et al. 1998, JQSRT, 60, 883
Pilbratt, G. L., Riedinger, J. R., Passvogel, T., et al. 2010, A&A, 518, L1
Planck, C., Ade, P. A. R., Aghanim, N., et al. 2016, A&A, 594, A28
Poglitsch, A., Waelkens, C., Geis, N., et al. 2010, A&A, 518, L2
Price-Whelan, A. M., Sipőcz, B. M., Günther, H. M., et al. 2018, AJ, 156, 123
Quénard, D., Jiménez-Serra, I., Viti, S., Holdship, J., & Coutens, A. 2018, MNRAS, 474, 2796
Rieke, G. H., Young, E. T., Engelbracht, C. W., et al. 2004, ApJS, 154, 25
Robitaille, T. P., Whitney, B. A., Indebetouw, R., & Wood, K. 2007, ApJS, 169, 328
Robitaille, T. P., Whitney, B. A., Indebetouw, R., Wood, K., & Denzmore, P. 2006, ApJS, 167, 256

Sahu, D., Liu, S.-Y., Su, Y.-N., et al. 2019, ApJ, 872, 196
Sahu, D., Liu, S.-Y., Liu, T., et al. 2021, ApJL, 907, L15
Saladino, R., Botta, G., Pino, S., Costanzo, G., & Di Mauro, E. 2012, Chem. Soc. Rev., 41, 5526
Siringo, G., Kreysa, E., Kovács, A., et al. 2009, A&A, 497, 945
Siringo, G., Kreysa, E., De Breuck, C., et al. 2010, Msngr, 139, 20
Stutz, A. M., Tobin, J. J., Stanke, T., et al. 2013, ApJ, 767, 36
Takahashi, S., & Ho, P. T. P. 2012, ApJL, 745, L10
Takahashi, S., Machida, M. N., Tomisaka, K., et al. 2019, ApJ, 872, 70
Taquet, V., Bianchi, E., Codella, C., et al. 2019, A&A, 632, A19
Tatematsu, K., Liu, T., Ohashi, S., et al. 2017, ApJS, 228, 12
Tatematsu, K., Liu, T., Kim, G., et al. 2020, ApJ, 895, 119
Tobin, J. J., Stutz, A. M., Megeath, S. T., et al. 2015, ApJ, 798, 128
Tobin, J. J., Sheehan, P. D., Megeath, S. T., et al. 2020, ApJ, 890, 130
van Gelder, M. L., Tabone, B., Tychoniec, Ł., et al. 2020, A&A, 639, A87
Watson, D. M. 2020, RNAAS, 4, 88
Werner, M. W., Roellig, T. L., Low, F. J., et al. 2004, ApJS, 154, 1
Whitney, B. A., Wood, K., Bjorkman, J. E., & Wolff, M. J. 2003, ApJ, 591, 1049
Wilson, T. L., & Rood, R. 1994, ARA&A, 32, 191
Wirström, E. S., Geppert, W. D., Hjalmarson, Å., et al. 2011, A&A, 533, A24
Wood, K., Wolff, M. J., Bjorkman, J. E., & Whitney, B. 2002, ApJ, 564, 887
Wright, E. L., Eisenhardt, P. R. M., Mainzer, A. K., et al. 2010, AJ, 140, 1868
Yang, Y.-L., Evans, N. J. I., Smith, A., et al. 2020, ApJ, 891, 61
Yang, Y.-L., Sakai, N., Zhang, Y., et al. 2021, ApJ, 910, 20
Yi, H.-W., Lee, J.-E., Liu, T., et al. 2018, ApJS, 236, 51
Zapata, L. A., Loinard, L., Rodríguez, L. F., et al. 2013, ApJL, 764, L14
Zucker, C., Speagle, J. S., Schlafly, E. F., et al. 2020, A&A, 633, A51